Early diversity in the firing pattern of embryonic Renshaw cells: just a synergy between two opposite voltage-dependent currents

Juliette Boeri[1¶], Claude Meunier[2¶], Hervé Le Corronc[1,3¶], Pascal Branchereau[4], Yulia Timofeeva[2,5,6], François Xavier Lejeune[7], Christine Mouffle[1], Hervé Arulkandarajah[1], Jean Marie Mangin[1], Pascal Legendre[1&], Antonny Czarnecki[1&]**

[1] INSERM, UMR_S 1130, CNRS, UMR 8246, Neuroscience Paris Seine, Institute of Biology Paris Seine, Sorbonne Univ, Paris, France.
[2] Centre de Neurosciences Intégratives et Cognition, CNRS UMR 8002, Institut Neurosciences et Cognition, Université de Paris, Paris, France.
[3] Univ Angers, Angers, France.
[4] Univ Bordeaux, INCIA, UMR 5287, Bordeaux, France.
[5] Department of Computer Science and Centre for Complexity Science, University of Warwick, Coventry, UK.
[6] Department of Clinical and Experimental Epilepsy, UCL Queen Square Institute of Neurology, University College London, London, UK.
[7] Institut du Cerveau et de la Moelle Epinière, Centre de Recherche CHU Pitié-Salpétrière, INSERM, U975, CNRS, UMR 7225, Sorbonne Univ, Paris, France.
* Corresponding authors
Email: pascal.legendre@inserm.fr (PL)
Email: antonny.czarnecki@sorbonne-universite.fr (AC)
[¶&]These authors contributed equally to this work.

Abstract

A remarkable feature of the developing central nervous system is the generation of spontaneous network activity (SNA) at the onset of synaptogenesis. In the spinal cord (SC) of the mouse embryo, SNA occurs around the 12th embryonic day (E12.5) and involves a recurrent functional loop between motoneurons (MNs) and GABAergic interneurons. We previously showed that Renshaw cells (V1^R), which constitute a functionally homogeneous population in the adult, are the first neurons enriched with GABA in the mouse embryonic lumbar SC. V1^R make synaptic-like contacts with MNs and likely participate to the genesis of SNA. However, how electrophysiological intrinsic properties of V1^R evolve during early development remains poorly understood. Here, using patch-clamp recordings, cluster analysis and biophysical modeling, we analyzed the mechanisms underlying the firing patterns of V1^R between E11.5 and E16.5. This developmental period covers the initial phase of development of SC activity (E11.5-E14.5) when SNA is present, and a pivotal period (E14.5-E16.5) when locomotor-like activity emerges. We discovered that V1^R can be subdivided into different clusters before E13.5 and that many cells are capable of sustaining repetitive firing or plateau potentials. These V1^R then lose transiently this firing ability, which is later recovered at E16.5. This is in contrast to the classical developmental scheme, i.e. an increase of firing capability with time. Combining pharmacology and computational modeling, we showed that the firing patterns of embryonic V1^R rely on the synergy between two opposing voltage-dependent currents, namely the slowly inactivating persistent sodium current and the delayed rectifier potassium current. These two currents are responsible for the repetitive firing of action potentials in a vast majority of neurons. Such a synergy is sufficient to explain the clustering of embryonic V1^R and determines the developmental trajectories of the electrical phenotype. Taken together our findings reveal a simple mechanism that is at the core of the heterogeneity of firing patterns. Such a mechanism must be tuned later on to eventually achieve firing pattern homogeneity.

Author summary

A remarkable feature of the developing central nervous system is the generation, at the onset of synaptogenesis, of a spontaneous network activity that is essential for the correct development of neuronal networks. Although the role of this early spontaneous network activity was extensively studied, little is known about the electrophysiological intrinsic properties of the key neurons involved in the genesis of this network activity. In the embryonic spinal cord, this activity involves a recurrent functional loop between motoneurons and GABAergic interneurons. We previously showed that embryonic Renshaw cells, known to control motoneurons firing in the mature spinal cord, are the first spinal neurons to produce GABA and likely participate to the genesis of the early spontaneous network activity. Using multiple approaches, including biophysical modeling, we found that, in contrast to the classical developmental scheme, Renshaw cells can be subdivided into different functional classes at the onset of network activity, and many cells are capable of sustaining repetitive firing or plateau potentials at this time; then they transiently lose this. We discovered that the firing patterns of these immature neurons rely on the synergy between two opposing voltage-dependent currents. Such a simple mechanism explains the functional diversity of embryonic Renshaw cells and determines the developmental trajectories of their electrical phenotype. Since these two voltage-gated currents are responsible for action potentials and are found in the vast majority of neurons, this basic mechanism is likely at the core of firing pattern heterogeneity. A tuning of this mechanism during later development, together with the involvement of a richer repertoire of voltage-dependent currents, is probably required to achieve the stereotypical firing patterns observed at the adult stage.

83 ## Introduction

84 The development of the central nervous system (CNS) follows complex steps, which
85 depend on genetic and environmental factors and involve interactions between multiple
86 elements of the neural tissue. Remarkably, emergent neurons begin to synchronize soon after
87 the onset of synapse formation, generating long episodes of correlated spontaneous network
88 activity (SNA), usually at low frequency (<0.01 Hz) [1-8]. In the mouse embryonic spinal
89 cord (SC), SNA is driven by an excitatory cholinergic-GABAergic loop between
90 motoneurons (MNs) and interneurons (INs), GABA being depolarizing before embryonic day
91 16.5 (E16.5) in the embryonic SC [9]. SNA emerges around E12.5 [4, 6, 10-12], at a time
92 when functional neuromuscular junctions are not yet established [13] and sensory and
93 supraspinal inputs have not yet reached the spinal motor networks [14-17].

94 Several studies pointed out that SNA is an essential component in neuronal networks
95 formation. [18-21]. In the SC, pharmacologically-induced disturbances of SNA between
96 E12.5 and E14.5 induce defects in the formation of motor pools, in motor axon guidance to
97 their target muscles and in the development of motor networks [4, 21-23]. This is consistent
98 with the proposition that emerging neural networks, although subject to constant changes,
99 must remain functionally stable to develop properly. During SNA episodes, long lasting giant
100 depolarization potentials (GDPs) are evoked in the SC, mainly by the massive release of
101 GABA onto MNs [12]. Renshaw cells ($V1^R$) are likely the first GABAergic partners of MNs
102 in the mouse embryo [24, 25], and the massive release of GABA during SNA probably
103 requires that many of them display repetitive action potential firing or plateau potential
104 activity [25].

105 However, little is known about the maturation of the intrinsic properties and the firing
106 pattern of embryonic $V1^R$ in the mouse embryo. We recently found that embryonic $V1^R$
107 exhibit heterogeneous excitability properties when SNA emerges in the embryonic SC [25] in

contrast to adult Renshaw cells that constitute a functionally homogeneous population [26, 27]. Whether this early functional diversity really reflects distinct functional classes of embryonic $V1^R$, how this diversity evolves during development, and what are the underlying biophysical mechanisms remain open questions. The impact of the functional diversity of embryonic $V1^R$ on MN activity during SNA episodes is also unknown. The present study addresses these issues using multiple approaches, including patch-clamp recordings, cluster analysis, biophysical modeling and dynamical systems theory. The firing patterns of embryonic $V1^R$ and the mechanisms underlying their functional diversity are analyzed during a developmental period covering the initial phase of development of SC activity in the mouse embryo (E11.5-E14.5), when SNA is present, and during the critical period (E14.5-E16.5), when GABAergic neurotransmission gradually shifts from excitation to inhibition and locomotor-like activity emerges [4, 10, 11].

Our study demonstrates that the heterogeneity of embryonic $V1^R$ found at E12.5 arises from the existence of distinct functional groups. Surprisingly, and in opposition to the classically accepted development scheme [28-33], we show that the embryonic $V1^R$ population loses its ability to support tonic firing from E13.5 to E15.5, exhibiting a transient functional involution during its development. Importantly, we highlight a simple biophysical mechanism, involving a synergy between two opposing voltage-dependent currents: the slowly inactivating subthreshold persistent sodium current (I_{Nap}) that shapes the firing pattern of neurons [34] and the delayed rectifier potassium current (I_{Kdr}), which accounts for the heterogeneity of embryonic $V1^R$. Because these two currents are ubiquitous in neurons, this basic mechanism could be at the core of firing pattern heterogeneity.

130 **Results**

131 ***The heterogeneity of the embryonic*** $V1^R$ ***firing patterns decreases during SC development.***

132 We previously highlighted that embryonic $V1^R$ are spontaneously active at E12.5. Their
133 response to a 2 s suprathreshold depolarizing current steps revealed four main patterns,
134 depending of the recorded interneuron. This led us to define four classes of $V1^R$ [25]: long-
135 lasting sodium-dependent plateau potentials (PP) $V1^R$, repetitive spiking (RS) $V1^R$, mixed
136 events (ME) $V1^R$ that shows an alternation of action potentials (APs) and plateau potentials,
137 and $V1^R$ firing only 1-3 APs at the onset depolarizing pulse, which were named single spiking
138 (SS) $V1^R$.

139 However, it was unclear whether these different firing patterns corresponded to well
140 separated classes within the E12.5 $V1^R$ population. To address this issue, we performed a
141 hierarchical cluster analysis on 163 embryonic $V1^R$, based on three quantitative parameters
142 describing the firing pattern evoked by a depolarizing pulse: the mean duration of evoked APs
143 or plateau potentials measured at half amplitude (mean ½Ad), the variability of the event
144 duration during repetitive firing (coefficient of variation of ½Ad: CV ½Ad) and the total
145 duration of all events, expressed in percentage of the pulse duration (depolarizing duration
146 ratio: ddr) (Fig 1A inserts). In view of the large dispersion of mean ½Ad and ddr values,
147 cluster analysis was performed using the (decimal) logarithm of these two quantities [35]. The
148 analysis of the distribution of log mean ½Ad, CV ½Ad and log ddr revealed multimodal
149 histograms that could be fitted with several Gaussians (S1 Fig, A1, B1 and C1). Cluster
150 analysis based on these three parameters showed that the most likely number of clusters was 5
151 (Fig 1, A and B), as determined by the silhouette width measurement (Fig 1B). Two clearly
152 separated embryonic $V1^R$ groups with CV ½Ad = 0 stood out, as shown in the 3D plot in Fig
153 1C (Fig 1C). The cluster with the largest ½Ad (mean ½Ad = 833.5 ± 89.99 ms) and the
154 largest ddr (0.441 ± 0.044) contained all PP $V1^R$ (n = 35) (Fig 1, C and D and S1 Fig, A2, B2

155 and C2). Similarly, the cluster with the shortest ½Ad (9.73 ± 0.66 ms) and the lowest ddr
156 (0.0051 ± 0.0004) contained all SS $V1^R$ (n = 46) (Fig 1, C and D and S1 Fig, A2, B2 and C2).
157 The three other clusters corresponded to $V1^R$ with nonzero values of CV ½Ad (Fig 1C). A
158 first cluster regrouping all RS $V1^R$ (n = 69) was characterized by smaller values of ½Ad
159 (23.91 ± 1.43 ms), CV ½Ad (27.36 ± 1.64%) and ddr (0.11 ± 0.01) (Fig 1, C and D and S1 Fig,
160 A2, B2 and C2). The last two clusters corresponded to ME $V1^R$ (Fig 1, C and D). The smaller
161 cluster, characterized by a larger CV ½Ad (170.9 ± 8.9%; n= 4), displayed a mix of APs and
162 short plateau potentials, while the second cluster, with smaller CV ½Ad (87.61 ± 7.37%; n =
163 9), displayed a mix of APs and long-lasting plateau potentials (Fig 1D and S1 Fig B2). Their
164 ½Ad and ddr values were not significantly different (S1 Fig, A2 and C2).
165 It must be noted that three embryonic $V1^R$ were apparently misclassified since they were
166 aggregated within the RS cluster although having zero CV ½Ad (Fig 1C; arrows).
167 Examination of their firing pattern revealed that this was because they generated only two
168 APs. However, their ddr (from 0.16 to 0.2) and ½ Ad values (from 31.6 to 40.3 ms) were well
169 in the range of values corresponding to the RS cluster. We cannot rule out that these rare
170 misclassified $V1^R$ (1.8%) actually constitute a sixth class of embryonic $V1^R$.
171 These different firing patterns of $V1^R$ might reflect different states of neuronal
172 development [29, 36-38]. During the development of neuron excitability single spiking and/or
173 plateau potentials are generally believed to be the most immature forms of firing pattern,
174 repetitive spiking being the most mature form [19, 39]. If it were so, firing patterns of
175 embryonic $V1^R$ would evolve during embryonic development from single spiking or plateau
176 potential to repetitive spiking, this latter firing pattern becoming the only one in neonates [26]
177 and at early postnatal stages [27]. RS neurons already represent 41% of $V1^R$ at E12.5. We
178 therefore analyzed the development of $V1^R$ firing patterns from E11.5, when they terminate
179 their migration and reach their final position [40], to E16.5. This developmental period covers

180 a first phase of development (E11.5-E14.5), where lumbar spinal networks exhibit SNA, and
181 a second phase (E14.5-E16.5), where locomotor-like activity begins [4, 11, 41, 42]. We first
182 analyzed changes in the intrinsic properties (input capacitance C_{in}, input resistance R_{in} =
183 $1/G_{in}$ and spike voltage threshold) of $V1^R$. Their capacitance C_{in} did not change significantly
184 from E11.5 to E13.5 (Fig 2A), remaining of the order of 12 pF, in agreement with our
185 previous work [25]. However, it increased significantly at the transition between the two
186 developmental periods (E13.5-E15.5) to reach about 23.5 pF at E15.5 (Fig 2A). A similar
187 developmental pattern was observed for R_{in}, which remained stable during the first phase
188 from E11.5 to E14.5 ($R_{in} \approx$ 1-1.2 GΩ) but decreased significantly after E14.5 to reach about
189 0.7 GΩ at E15.5 (Fig 2B). Spike threshold values also decreased significantly between the
190 first and the second developmental phases, dropping from about -34 mV at E12.5 to about -41
191 mV at E16.5 (Fig 2C). Interestingly, this developmental transition around E14.5 correspond to
192 the critical stage at which SNA gives way to a locomotor-like activity [11, 41, 42] and
193 rhythmic activity becomes dominated by glutamate release rather than acetylcholine release
194 [4].

195 This led us to hypothesize that this developmental transition could be also critical for the
196 maturation of embryonic $V1^R$ firing patterns. The distinct $V1^R$ firing patterns observed at
197 E12.5 were already present at E11.5 (Figs 1D and 3A), but the percentage of RS $V1^R$ strongly
198 increased from E11.5 to E12.5, while the percentage of ME $V1^R$ decreased significantly (Fig
199 3F). The heterogeneity of $V1^R$ firing patterns substantially diminished after E12.5. Plateau
200 potentials were no longer observed at E13.5, and ME $V1^R$ disappeared at E14.5 (Fig 3, B, C
201 and F). Interestingly, the proportion of SS $V1^R$ remained high from E13.5 to E15.5 and even
202 slightly increased (91.23% at E14.5 and 93.33% at E15.5; Fig 3F). This trend was partially
203 reversed at E16.5, as the percentage of RS $V1^R$ increased at the expense of SS $V1^R$ (67.86 %
204 SS $V1^R$ and 32.34% RS $V1^R$; Fig 3F). This decrease in repetitive firing capability after E13.5

205 was surprising in view of what is classically admitted on the developmental pattern of
206 neuronal excitability [18, 43]. Therefore, we verified that it did not reflect the death of some
207 embryonic $V1^R$ after E13.5. Our data did not reveal any activated caspase3 (aCaspase3)
208 staining in VI^R (FoxD3 staining) at E14.5 (n = 10 SCs) (Fig 4), in agreement with previous
209 reports showing that developmental cell death of $V1^R$ does not occur before birth [44].
210

211 ***The voltage-dependent potassium delayed rectifier current I_{Kdr} is a key partner of the***
212 ***persistent sodium current I_{Nap} in controlling embryonic $V1^R$ firing patterns during***
213 ***development.***

214 In our previous work we discovered a relationship between I_{Nap} and the ability of
215 embryonic $V1^R$ to sustain repetitive firing [25]. However, the heterogeneous firing patterns
216 of $V1^R$ observed at E12.5 could not be fully explained by variations in I_{Nap} [25]. It is
217 therefore likely that other voltage-gated channels, such as potassium channels, known to
218 control firing and AP repolarization, play a role in the control of the firing pattern of $V1^R$. Our
219 voltage clamp protocol did not reveal any inward rectifying current at E12.5 nor at E14.5
220 (hyperpolarizing voltage steps to -100 mV from V_H = -20 mV, data not shown), but we found
221 two voltage-dependent outward potassium currents, a delayed rectifier current (I_{Kdr}) and a
222 transient potassium current (I_A) in embryonic $V1^R$, whatever the firing pattern (Fig 5). These
223 two currents are known to control AP duration and/or firing pattern [45]. The activation
224 threshold of I_{Kdr} lied between -30 mV and -20 mV and the threshold of I_A between -60 mV
225 and -50 mV, (n = 27) (Fig 5, A2, A4, A6 and B2).

226 It is unlikely that the heterogeneity of $V1^R$ firing patterns results from variations in the
227 intensity of I_A, because its voltage-dependent inactivation (time constant: 23.3 ± 2.6 ms, n =
228 8), which occurs during the depolarizing phase of an AP, makes it ineffective to control AP or

229 plateau potential durations. This was confirmed by our theoretical analysis (see S2 Fig). We
230 thus focused on I_{Kdr}.

231 At E12.5 PP V1^R had a significantly lower G_{Kdr} (2.12 ± 0.44 nS, n = 6) than SS V1^R (5.57
232 ± 0.56 nS, n = 9) and RS V1^R (6.39 ± 0.83 nS, n = 7) (Fig 6A). In the same manner, PP V1^R at
233 E12.5 had a significantly lower G_{Kdr} than SS V1^R at E14.5 (11.11 ± 1.12 nS, n = 10).
234 However, there was no significant difference in G_{Kdr} between SS V1^R and RS V1^R at E12.5
235 (Fig 6A), which indicated that variations in G_{Kdr} alone could not explain all the firing patterns
236 observed at E12.5.

237 Similarly, there was no significant difference in G_{Nap} between RS V1^R (0.91 ± 0.08 nS, n =
238 8) and PP V1^R (1.24 ± 0.19 nS, n = 6) at E12.5 (Fig 6B), indicating that variations
239 in G_{Nap} alone could not explain all the firing patterns of V1^R at E12.5 [25]. G_{Nap} measured in
240 SS V1^R at E12.5 (0.21 ± 0.06 nS, n = 9) (Fig 6B) and in SS V1^R at E14.5 (0.13 ± 0.05 nS, n =
241 10) (Fig 6B and S3 Fig) were significantly lower compared to G_{Nap} measured in RS V1^R and
242 in PP V1^R at E12.5 (Fig 6B). This suggests that repetitive firing and plateaus require a
243 minimal I_{Nap} intensity.

244 Because the firing pattern of a neuron depends on the balance between outward currents
245 and inward voltage-dependent currents [45], we then hypothesized that the different firing
246 patterns of V1^R observed at E12.5 were related to the G_{Nap} / G_{Kdr} ratio. We found that this
247 ratio was significantly lower for SS V1^R recorded at E12.5 (G_{Nap} / G_{Kdr} = 0.043 ± 0.015, n =
248 9) or at E14.5 (0.012 ± 0.004, n = 10) compared to RS V1^R (0.154 ± 0.022, n = 8) and PP V1^R
249 (0.66 ± 0.132, n = 6) recorded at the same age (Fig 6C). We also found that
250 the G_{Nap} / G_{Kdr} ratio was significantly lower for RS V1^R compared to PP V1^R (Fig 6C).

251 Altogether, these results strongly suggest that, although the presence of I_{Nap} is required
252 for embryonic V1^R to fire repetitively or to generate plateau potentials [25], the heterogeneity

253 of the firing pattern observed between E12.5 and E14.5 is not determined by I_{Nap} *per se* but
254 by a synergy between I_{Nap} and I_{Kdr}.
255
256 ***Manipulating the balance between G_{Nap} and G_{Kdr} changes embryonic V1^R firing patterns.***
257 We previously showed that blocking I_{Nap} with riluzole converted PP V1^R or RS V1^R into
258 SS V1^R [25]. To confirm further that the balance between G_{Nap} and G_{Kdr} was the key factor
259 that determined the heterogeneity of V1^R firing patterns, we assessed to what extent a given
260 SS V1^R cell could change its firing pattern when I_{Kdr} was gradually blocked by 4-
261 aminopiridine (4-AP). We found that I_{Kdr} could be blocked by microM concentrations of 4-
262 AP (Fig 7) without affecting I_A at E12.5 and E14 .5 (S4 Fig A). This result favors the presence
263 of the potassium channel subunit $K_{V3.1}$ [46, 47], which is known to be also present at postnatal
264 stages [48], in V1^R both at E12.5 and E14.5.
265 To assess to what extent we could alter the balance between I_{Nap} and I_{Kdr}, we had to
266 determine first the dose-response curve of I_{Kdr} inhibition by 4-AP. 4-AP, applied at
267 concentrations ranging from 0.3 μM to 300 μM, specifically inhibited I_{Kdr} (Fig 7, A1 and A2)
268 with an IC_{50} of 2.9 μM (Fig 7B), without significantly affecting I_A (S4 Fig, A). We then
269 determined to what extent increasing the concentration of 4-AP modified the firing pattern of
270 embryonic V1^R at E12.5. Applying 4-AP at concentrations ranging from 3 μM to 300 μM
271 changed the firing pattern of SS V1^R recorded at E12.5 (n = 10) in a concentration-dependent
272 manner (Fig 8, A1, A2 and A3). In 50% of the recorded embryonic V1^R, increasing 4-AP
273 concentrations successfully transformed SS V1^R into PP V1^R with the following sequence: SS
274 → RS → ME → PP (Fig 8A1). In a second group of embryonic V1^R (25%), 4-AP application
275 only evoked mixed activity, with the same sequence as aforementioned (SS → RS → ME). In
276 the remaining SS V1^R (25%), increasing 4-AP concentration only led to sustained AP firing
277 (Fig 8A2). Application of 300 μM 4-AP on RS V1^R at E12.5 evoked mixed events or plateau

278 potentials (S5 Fig). Plateau potentials and repetitive spiking evoked in the presence of 300
279 μM 4-AP were fully blocked by 0.5-1 μM TTX, indicating that they were generated by
280 voltage-gated Na^+ channels (Fig 8, A4 and A5 and S5 Fig).

281 At E14.5, 300 μM 4-AP inhibited only 59.2% of I_{Kdr}. Increasing 4-AP concentration to
282 600 μM did not inhibit I_{Kdr} significantly more (60.2%) (S6 Fig), indicating that inhibition of
283 I_{Kdr} by 4-AP reached a plateau at around 300 μM. 600 μM 4-AP application had no
284 significant effect on I_A (S4 Fig).

285 The application of the maximal concentration of 4-AP tested (600 μM) converted SS $V1^R$
286 (n = 13) to PP $V1^R$ (23.1%; Fig 8, B1 and B3), RS $V1^R$ (38.5% Fig 8, B2 and B3) or ME $V1^R$
287 (38.4%; Fig 8B3), as was observed at E12.5, thus indicating that the firing pattern of
288 embryonic $V1^R$ depends on the balance between I_{Nap} and I_{Kdr} also at E14.5. Plateau potential
289 and repetitive spiking recorded in the presence of 4-AP at E14.5 were fully blocked by 0.5-1
290 μM TTX indicating that they were generated by voltage-gated Na^+ channels (Fig 8, B1 and
291 B2), as observed at E12.5. It should be noted that the application of 300 μM of 4-AP induced
292 a significant 30.5 ± 12.4 % increase (P = 0.0137; Wilcoxon test) in the input resistance of the
293 recorded cells (1.11 ± 0.08 GΩ versus 1.41 ± 0.12 GΩ; n = 11).

294 These results show that, in addition to I_{Nap}, the delayed rectifier potassium current is also a
295 major determinant of the firing pattern of embryonic $V1^R$. They suggest that the firing pattern
296 depends on a synergy between I_{Nap} and I_{Kdr} and that the different patterns can be ordered
297 along the following sequence SS → RS → ME → PP when the ratio $G_{Nap}/\ G_{Kdr}$ is increased.

298

299 ***Theoretical analysis: basic model.***

300 As shown in Fig 9A for 26 cells, in which both G_{Nap} and G_{Kdr} were measured, the three
301 largest clusters revealed by the hierarchical clustering analysis (SS, RS and PP, which account
302 together for the discharge of more than 95% of cells, see Fig 1) correspond to well defined

303 regions of the G_{Nap}- G_{Kdr} plane. Single spiking is observed only when G_{Nap} is smaller than
304 0.6 nS. For larger values of G_{Nap}, repetitive spiking occurs when G_{Kdr} is larger than 3.5 nS,
305 and $V1^R$ display plateau potentials when G_{Kdr} is smaller than 3.5 nS. Mixed events (ME, 4.5%
306 of the 163 cells used in the cluster analysis), where plateaus and spiking episodes alternate,
307 are observed at the boundary of RS and PP clusters. This suggested to us that a conductance-
308 based model incorporating only the leak current, I_{Nat}, I_{Nap} and I_{Kdr} (see Materials and
309 Methods) could account for the experimental observations, the observed zonation being
310 explained in terms of bifurcations between the different stable states of the model.

311 A one-parameter bifurcation diagram of the model is shown in Fig 9B for two values of
312 G_{Kdr} (2.5 nS and 10 nS) and a constant injected current I = 20 pA. The slow inactivation of
313 I_{Nap} was not taken into account at this stage of our analysis. For G_{Kdr} = 10 nS, the steady-
314 state membrane voltage progressively increases (in gray) with G_{Nap}, but repetitive spiking (in
315 red, see voltage trace for G_{Nap}= 1.5 nS) is not achieved until G_{Nap} reaches point SN_1, where a
316 saddle node (SN) bifurcation of limit cycles occurs. This fits with the experimental data,
317 where a minimal value of G_{Nap} is required for repetitive spiking (see also [25]), and is in
318 agreement with the known role of I_{Nap} in promoting repetitive discharge [49, 50]. Below SN_1,
319 the model responds to the onset of a current pulse by firing only one spike before returning to
320 quiescence (see voltage trace for G_{Nap}= 0.1 nS), or a few spikes when close to SN_1 (not
321 shown). The quiescent state becomes unstable through a subcritical Hopf bifurcation (HB) at
322 point HB_1, bistability between quiescence and spiking occurring between SN_1 to HB_1.
323 Repetitive firing persists when G_{Nap} is increased further and eventually disappears at point
324 SN_2. The firing rate does not change much throughout the RS range (see S2 Fig B), remaining
325 between 11.9 Hz (at SN_1) and 17.1 Hz (at SN_2). A stable plateau appears at point HB_2 through

326 a subcritical HB. The model is bistable between HB_2 and SN_2, where both plateau and large
327 amplitude APs coexist.

328 The model behaves very differently when G_{Kdr} is reduced to 2.5 nS (gray-blue curve in
329 Fig 9B). It exhibits a unique stable fixed point whatever the value of G_{Nap} is, and the
330 transition from quiescence to plateau is gradual as G_{Nap} is increased. No repetitive spiking is
331 ever observed. This indicates that the activity pattern is controlled not only by G_{Nap} but also
332 by G_{Kdr}. This is demonstrated further in Fig 9C, where G_{Nap} was fixed at 1.5 nS while G_{Kdr}
333 was increased from 0 to 25 nS. The model exhibits a plateau potential until G_{Kdr} is increased
334 past point HB_2. Repetitive spiking then sets in, *via* a supercritical HB (in contrast to the
335 subcritical bifurcation in Fig 9B for G_{Kdr} = 10 nS, see legend of Fig 9). The amplitude of AP
336 decays to zero at HB_2, and no bistability occurs. When G_{Kdr} is further increased, repetitive
337 firing eventually disappears through a SN bifurcation of limit cycles at point SN_1, the
338 quiescent state becomes stable through a subcritical HB at point HB_1, and bistability occurs
339 between these two points. This behavior is in agreement with Fig 9A.

340 Since both G_{Nap} and G_{Kdr} control the firing pattern of embryonic $V1^R$ cells, we computed a
341 two-parameters bifurcation diagram (Fig 9D), where the different possible activity states and
342 the transitions between them are plotted in the G_{Nap} - G_{Kdr} plane. The black lines correspond
343 to the bifurcations HB_1 and HB_2 and delimit a region where only repetitive firing occurs. The
344 red lines correspond to the SN bifurcations of periodic orbits associated with the transition
345 from quiescence to firing (SN_1) and the transition from plateau to firing (SN_2). They
346 encompass a region (shaded area) where repetitive firing can be achieved but possibly
347 coexists with quiescence (between the HB_1 and SN_1 lines) or plateau potential (in the narrow
348 region between the HB_2 and SN_2 lines). We note that the SN_1 and SN_2 lines merge with the
349 HB_1 and HB_2 lines at points B_1 and B_2, respectively. There, codimension-two Bautin

350 bifurcations occur, and the bifurcations HB_1 and HB_2 switch from subcritical to supercritical
351 case.

352 Some important features of the diagram must be emphasized: 1) minimal values of both
353 G_{Nap} (to ensure sufficient excitability) and G_{Kdr} (to ensure proper spike repolarization) are
354 required for repetitive spiking, 2) quiescence and plateau can be clearly distinguished only
355 when they are separated by a region of repetitive spiking (see also Fig 9B for G_{Kdr}= 10 nS),
356 otherwise the transition is gradual (see also Fig 9B for G_{Kdr}= 2.5 nS), 3) only oblique lines
357 with an intermediate slope cross the bifurcation curve and enter the RS region (see, for
358 example, the red line in Fig 9D). This means that repetitive spiking requires an appropriate
359 balance between I_{Nap} and I_{Kdr}. If the ratio G_{Nap}/G_{Kdr} is too large (blue line) or too small
360 (gray line), only plateau potentials or quiescence will be observed at steady state. This is
361 exactly what is observed in experiments, as shown by the cumulative distribution function of
362 the ratio G_{Nap}/G_{Kdr} for the different clusters of embryonic $V1^R$ in Fig 9E (same cells as in A).
363 The ratio increases according to the sequence SS → RS → ME → PP, with an overlap of the
364 distributions for SS $V1^R$ and RS $V1^R$. Note also that the ratio for ME cells (around 0.25)
365 matches the transition between repetitive spiking and plateau potentials in D (more on this
366 below).

367 Embryonic $V1^R$ cells display voltage fluctuations of up to 5 mV, presumably due to
368 channel noise. The relatively low number of sodium and potassium channels (of the order of a
369 few thousands) led to voltage fluctuations in the stochastic version of our model comparable
370 to those seen experimentally when the cell was quiescent (top voltage trace in Fig 9D) or
371 when a voltage plateau occurred (bottom trace). Channel noise caused some jitter during
372 repetitive spiking (middle trace), with some occasionally missing spikes (not shown), and
373 induced clearly visible variations in the amplitude of APs. However, repetitive firing proved
374 to be very robust and was not disrupted by voltage fluctuations. Altogether, channel noise

375 little alters the dynamics (compare the deterministic voltage traces in Fig 9B and the noisy
376 traces in Fig 9D). This is likely because channel noise has a broad power spectrum and did
377 not resonate with the deterministic solutions of the model.

378 The one-parameter bifurcation diagram of our model was not substantially modified when
379 we took I_A into account, as shown in S2 Fig. It just elicited a slight membrane
380 hyperpolarization, a rightward shift of the firing threshold and a decrease of the firing
381 frequency. The transition from repetitive firing to plateau was not affected because I_A is
382 inactivated by depolarization.

383 The bifurcation diagram of Fig 9D accounts for the physiological data on $V1^R$ at E12.5
384 presented in Fig 9A, as shown in Fig 9E where the conductance data of Fig 9A were
385 superimposed on it. Its exact position in the G_{Nap} - G_{Kdr} plane actually depends on the values
386 of the passive parameters and it was computed in Fig 9D and F for G_{in}= 1 nS and C_{in}= 13 pF,
387 the median values of the input capacitance and conductance at E12.5. Between E12.5 and
388 E14.5, C_{in}, which provides an estimate of the cell size, increases by 38% in average, whereas
389 the input conductance G_{in} is not significantly modified (see Fig 2). As illustrated in Fig 9G
390 the two-parameters bifurcation diagram is then shifted upward and rightward compared to Fig
391 9F, because larger conductances are required to obtain the same firing pattern. The observed
392 regression of excitability from E12.5 to E14.5-E15.5 (see Fig 3) thus comes from a decrease
393 in G_{Nap} density (see presumable developmental trajectories indicated by arrow in F) together
394 with a shift of the RS region as cell size increases. As a result, all 9 cells shown in Fig 9G are
395 deeply inside the SS region at E14.5.

396 The bifurcation diagram of Fig 9D and F cannot readily account for the experiments where
397 decreasing G_{Kdr} with 4-AP changed the firing pattern of SS $V1^R$ (see Fig 8). This is because
398 4-AP decreases substantially the input conductance, which leads to a decreased rheobase
399 current. If we take these changes in the passive parameters into account (see S7 Fig), the

400 bifurcation diagram remains qualitatively the same, but it is shifted toward the origin in the
401 G_{Nap}- G_{Kdr} plane. As a consequence, the bifurcation lines between SS and RS (SN1) and
402 between RS and PP (SN2) are successively crossed when G_{Kdr} is reduced, in accordance with
403 experimental results.
404
405 ***Theoretical analysis: extended model with slow inactivation of the persistent sodium***
406 ***current.***
407 Our basic model accounts for the firing pattern of 73% of the 163 cells used in the cluster
408 analysis. However, bursting, under the form of recurring plateaus separated by brief
409 repolarization episodes (see a typical trace in Fig 10A left), was experimentally observed in
410 half of PP $V1^R$ (24 out of 46) and plateaus intertwined with spiking episodes were recorded in
411 the 13 cells of the ME cluster (8% of the total sample, see Fig 10A right for an example).
412 Recurrent plateaus indicate membrane bistability. This requires that the $I - V$ curve be S-
413 shaped, which occurs when anomalous rectification is large (large G_{Nap} and small G_{Kdr} , Fig
414 10, B1 and B2). However, our basic model lacks a mechanism for switching between
415 quiescent state and plateau. Channel noise might induce such transitions, but our numerical
416 simulations showed that this is too infrequent to account for bursting (see voltage trace in Fig
417 10B1 where the plateau state is maintained despite channel noise).

418 To explain recurrent plateaus, we incorporated a slow dynamical process, namely the
419 experimentally observed slow inactivation of G_{Nap}, in our model. The one-parameter
420 bifurcation diagram of the basic model for G_{Kdr} = 2.5 nS is shown in Fig 10C. The injected
421 current was reduced from the value of 20 pA used in the previous section to 8 pA , so as to
422 allow for bistability (Fig 10B2). The $G_{Nap} - V$ curve is then S-shaped, as shown in Fig 10B1,
423 with a bistability region for G_{Nap} between 1.48 and 1.87 nS. This is in contrast with Fig 9B

424 where the $G_{Nap} - V$ curve was monotonic. Adding slow (de)inactivation of I_{Nap} caused
425 periodic transitions between up (plateau) and down (quiescent) states, and the model then
426 displayed a stable limit cycle (shown in black in Fig 10C), as illustrated by the top voltage
427 trace on the right. This mechanism is known as pseudo-plateau bursting (a.k.a. fold-subcritical
428 HB bursting) [51]. It is akin to square wave bursting [52-55], but the up-state is a stable fixed
429 point rather than a limit cycle [56-58], which is why recurrent plateaus are obtained rather
430 than bursts of APs. The duration of the plateaus and repolarization episodes depends on the
431 values of G_{Nap}, G_{Kdr} and I, but it is also largely controlled by the inactivation kinetics. A
432 voltage-independent time constant τ_s leads to up and down states of comparable durations
433 (see top voltage trace in Fig 10C), the duration of which increases with τ_s. Making τ_s voltage-
434 dependent changes the relative durations of plateaus and repolarization episodes. If τ_s
435 decreases with membrane voltage, for instance, repolarization episodes are shortened (bottom
436 voltage trace). Adding channel noise preserves bursting but introduces substantial randomness
437 in the duration of plateaus and repolarization episodes (middle voltage trace). We also noted
438 that adding the I_A current lengthened the repolarizing phase (S2 Fig).

439 Slow inactivation of the persistent sodium current also provides an explanation for mixed
440 patterns, where plateaus alternate with spiking episodes (Fig 10A, right). They take place in
441 our model near the transition between repetitive spiking and plateau, as in experiments (see
442 Fig 9A). Slow inactivation (V_s = -30 mV, k_s = -5 mV) may then lead to elliptic bursting [59,
443 60] when the bifurcation HB_2 is subcritical and located near the Bautin bifurcation B_2, which
444 is the case here (Fig 9D). The model then displays a stable limit cycle with alternating
445 plateaus and spiking episodes, arising from crossing the bifurcation points HB_2 and SN_2 back
446 and forth (see bifurcation diagram in Fig 10D and top voltage trace). We note that sufficient
447 deinactivation of I_{Nap} for triggering a new plateau is difficult to be achieved during spiking
448 episodes, because voltage oscillates over a large range and variations of the inactivation level

449 are largely averaged out. Therefore, we had to choose a shallower inactivation curve than for
450 pseudo-plateau bursting together with a more depolarized half-inactivation voltage to achieve
451 elliptic bursting. Otherwise, the model keeps on spiking repetitively without returning to the
452 plateau state. This is probably why it is difficult in many recorded cells to elicit plateaus by
453 increasing the injected current, an experimental observation that was not explained by our
454 basic model.

455 When τ_s is voltage-dependent and small enough in the subthreshold voltage range, there is
456 not enough time for APs to be fired between plateaus (see bottom voltage trace in Fig 10D).
457 One then observes successive plateaus with superimposed voltage oscillations that decay at
458 plateau onset and grow at offset. Both types of plateaus, with voltage oscillations (elliptic
459 bursting) and without (pseudo-plateau bursting) are observed in recorded embryonic $V1^R$.
460 Finally, we note that bistability between plateau and repetitive spiking is not necessary for
461 elliptic bursting, which may also be due to the slow passage through HB_2 when this Hopf
462 bifurcation is supercritical [61, 62]. Slow inactivation of I_{Nap} then leads to a delayed
463 destabilization of the plateau after HB_2 is crossed, while deinactivation during repetitive
464 spiking leads to the crossing of HB_2 in the opposite direction and a delayed restabilization of
465 the plateau (not shown).

466 Altogether, our study shows that a model incorporating the slow inactivation of
467 I_{Nap} accounts for all the firing patterns displayed by cells of the PP and ME clusters.

468

469 ***Effect of evoked changes of GABAergic interneuron firing pattern using 4-AP on evoked-***
470 ***GABAergic response on MNs at E12.5.***

471 During SNA, MNs receive massive inputs from GABAergic INs and, to a lesser extent,
472 from glutamatergic INs. This leads to the occurrence of GDPs [12]. We previously showed
473 that embryonic $V1^R$ are likely the first INs to release GABA in E12.5 SC [25]. Even though

474 I_{Nap} appears essential for the occurrence of GDPs and SNA in the SC at E12.5 [25], it is
475 unclear how the heterogeneity of the activity patterns observed in $V1^R$ shapes GABA-evoked
476 current in MNs. To address this issue, we took advantage of the ability of 4-AP to change the
477 activity pattern of $V1^R$. We focused our analysis on the evoked GABAergic Giant Inward
478 Currents (GICs) (voltage clamp recordings; E_{Cl} = -30 mV) and GABAergic Giant
479 Depolarizing Potential (GDPs) (current clamp recordings). GICs and GDPs were induced by a
480 1 ms stimulation applied at the cervical level of the SC while recording lumbar MNs (Fig 11A)
481 in the presence of the broad spectrum glutamate receptor antagonist kynurenic acid (4 mM).
482 At E12.5, 4-AP increased the amplitude of GABAergic GICs (155 ± 86 pA vs 191 ± 112 at 30
483 μM, and 206 ± 115 pA at 300 μM, n = 6) and the GICs half-width (0.57 ± 0.28 s vs 1.01 ±
484 0.34 s at 30 μM, and 1.32 ± 0.34 s at 300 μM, n = 6) (Fig 11, B1 and B2). When analyzing
485 GDPs, we observed a strong increase of their half-width in the presence of 4-AP (1.9 ± 0.4 s
486 vs 3.8 ± 1.3 s at 30 μM, and 3.6 ± 1.1 s at 300 μM, n = 8) but no significant change in their
487 amplitude (30.5 ± 7.2 mV vs 32.6 ± 6.4 mV at 30 μM and 33.4 ± 7.2 mV at 300 μM, n = 8),
488 nor in the firing rate of MNs (Fig 11, C1 and C2). Increasing the proportion of GABAergic
489 INs that sustain repetitive firing or plateau potential activity likely enhances the release of
490 GABA on MNs as exemplified by the increased evoked GABAergic current on MNs.
491 However lack of effects on GDP amplitude and on MN firing also indicates that biophysical
492 properties of MNs likely buffer variations in the intensity of their GABAergic inputs. This is
493 likely due to a combination of the depolarized equilibrium potential of chloride at this
494 embryonic age (ECl = -30 mV; [9]) and the relatively high input resistance of E12.5 MNs
495 (0.3-1 GΩ) [12]), allowing relatively small changes in GABAergic conductance to evoke a
496 voltage response with maximum amplitude. Such a process probably contributes to the
497 robustness of MN activity during episodes of SNA.

498 ## Discussion

499 $V1^R$ constitute a homogeneous population in terms of their transcription factor program
500 expressed during development [24, 63], their physiological function [64] and their firing
501 pattern in postnatal stages [27]. Surprisingly, our electrophysiological recordings and our
502 cluster analysis clearly indicate that distinct functional classes of $V1^R$ are transiently present
503 during development at the onset of the SNA (E11.5-E12.5). Five different groups of
504 embryonic $V1^R$ were defined using cluster analysis, according to their firing properties.

505

506 ***Development of the firing pattern of embryonic $V1^R$ during SNA.***

507 It is generally assumed that, during early development, newborn neurons cannot sustain
508 repetitive firing [33, 43]. Later on, neurons progressively acquire the ability to fire repetitively,
509 APs become sharper, and neurons eventually reach their mature firing pattern, due to the
510 progressive appearance of a panoply of voltage-gated channels with different kinetics [18, 33,
511 43]. Our results challenge the general view that single spiking is a more immature form of
512 excitability [33]. Indeed, we show that repetitive firing and plateau potentials dominate at
513 early stages (E11.5-E12.5), single spiking prevailing only later (E13.5- E16.5).

514 The functional heterogeneity of embryonic $V1^R$ is unlikely to be a special case during the
515 early development of neuronal excitability. Firing pattern heterogeneity was also observed in
516 the mouse enteric nervous system at E11.5-E12.5 [65] and in SC rat MNs at early postnatal
517 ages [66, 67]. The different $V1^R$ firing patterns observed at E11.5-E12.5 might reflect
518 variability in the maturation level between $V1^R$ at a given developmental stage, as suggested
519 for developing MNs [67]. If so, the proportion of $V1^R$ that can sustain repetitive firing would
520 be expected to increase with age, but this is not the case. The transient functional
521 heterogeneity of embryonic $V1^R$ rather reflects an early developmental stage of intrinsic

522 excitability, occurring before the increase in the diversity of voltage-gated ion channels
523 stabilizes a robust mature firing pattern [68].

524 The physiological meaning of this transient functional involution of embryonic $V1^R$ is
525 puzzling. To our knowledge, such a phenomenon was never described in vertebrates during
526 CNS development. So far, a functional involution was described only for inner hair cells
527 between E16 and P12 [69, 70] and cultured oligodendrocytes [71], and it was irreversible.
528 Because most embryonic $V1^R$ cannot sustain tonic firing after E12.5, it is likely that their
529 participation to SNA is limited to the developmental period before other GABAergic
530 interneuron subtypes mature and start to produce GABA and glycine [72]. Interestingly,
531 embryonic $V1^R$ begin to recover their capability to sustain tonic firing when locomotor-like
532 activity emerges [4, 11], a few days before they form their recurrent synaptic loop with MNs
533 (around E18.5 in the mouse embryos, [73]). One possible function of this transient involution
534 could be to regulate the growth of embryonic $V1^R$ axons toward their targets. It is indeed
535 known that low calcium fluctuations within growth cones are required for axon growth while
536 high calcium fluctuations stop axon growth and promote growth cone differentiation [74].

537

538 ***Ion channels mechanisms underlying embryonic $V1^R$ functional heterogeneity.***

539 The heterogeneous discharge patterns of embryonic $V1^R$ contrasts with the unique firing
540 pattern of $V1^R$ at postnatal age [27] and likely reflects immature properties. Blockade of
541 I_{Nap} leads to single spiking [25], which emphasizes the importance of this current for the
542 occurrence of repetitive firing and plateau potentials in $V1^R$ at early development stages. But
543 these neurons can also switch from one firing pattern to another, when G_{Kdr} is decreased by
544 4-AP, which emphasizes the importance of I_{Kdr}. We found that the main determinant of
545 embryonic $V1^R$ firing pattern is the balance between G_{Nap} and G_{Kdr}.

546 A Hodgkin-Huxley-like model incorporating a persistent sodium current I_{Nap} provided a
547 parsimonious explanation of all the firing patterns recorded in the $V1^R$ population at E12.5,
548 even in details. It provided a mathematical interpretation for the clustering of embryonic $V1^R$
549 shown by the hierarchical analysis and accounted for the effect of 4-AP and riluzole [25] on
550 the discharge. Remarkably, it highlights how a simple mechanism involving only the two
551 opposing currents I_{Nap} and I_{Kdr} can produce functional diversity in a population of
552 developing neurons. The model explains why minimal G_{Nap} and G_{Kdr} are required for firing,
553 how a synergy between G_{Nap} and G_{Kdr} controls the firing pattern, and it accounts for the
554 zonation of the $G_{Nap} - G_{Kdr}$ plane that is observed experimentally.

555 Adding the slow inactivation of I_{Nap} to the model allowed us to account for the bursting
556 patterns displayed by cells of the PP and ME clusters. We showed, in particular, that mixed
557 events arose from elliptic bursting at the repetitive spiking-plateau transition and that smooth
558 repetitive plateaus could be explained by a pseudo-plateau bursting mechanism [51, 57]. Such
559 bursting scenario has been previously studied in models of endocrine cells [56, 75, 76] and
560 adult neurons [77], but rarely observed in experiments. Heterogeneity of pacemaker neurons
561 discharge pattern has also been observed in the embryonic pre-Bötzinger network [78].
562 However, it is related to the gradual change of a balance between two inward currents,
563 I_{Nap} and the calcium-activated nonselective cationic current I_{CAN}, during neuronal maturation,
564 which leads to the progressive replacement of pseudo-plateau bursting by elliptic bursting.
565 Such a scenario cannot account for the variety of discharge patterns observed in embryonic
566 $V1^R$ at the E11.5-12.5 stage of development [25]. Our theoretical analysis and our
567 experimental data clearly indicate that competition and synergy between two opposing
568 currents are necessary to explain all the firing patterns of $V1^R$. We also note that our model is
569 not restricted to embryonic $V1^R$, but may also apply to any electrically compact cell, the firing

570 activity of which is dominated by sodium and delayed rectifier potassium currents. This is the
571 case of many classes of embryonic cells in mammals at an early stage of their development.
572 Altogether our experimental and theoretical results provide a global view of the
573 developmental trajectories of embryonic $V1^R$ (see Fig 9, F and G). At E12.5, conductances of
574 embryonic $V1^R$ are widely spread in the $G_{Nap} - G_{Kdr}$ plane, which explains the heterogeneity
575 of their firing patterns. This likely results from the random and uncorrelated expression of
576 sodium and potassium channels from cell to cell at this early stage. Between E12.5 and E14.5-
577 15.5 cell size increases, and G_{Kdr} with it, while the density of sodium channels decreases (see
578 Figs 6 and 9). The functional involution displayed by $V1^R$ between E12.5 and E15.5 thus
579 results from a decrease of G_{Nap} coordinated with an increase of G_{Kdr} as cells grow. How
580 these two synergistic processes are controlled during this developmental period remains an
581 open issue.
582
583 ***Functional implication of embryonic $V1^R$ firing pattern heterogeneity at the onset of the***
584 ***SNA.***
585 The increase in GABAergic GIC amplitude and duration in the presence of 4-AP suggests
586 that 4-AP, by increasing embryonic $V1^R$ excitability, augments GABA release onto MNs.
587 This fits with the view according to which repetitive firing is more efficient than single
588 spiking to evoke presynaptic calcium entry and promote vesicular release at presynaptic
589 terminals, plateau potentials being even more efficient [79-81]. This is also consistent with
590 our previous results [25] showing that repetitive firing, mixed event activity or plateau
591 potential activity were required for GABAergic GICs to occur on MNs. We cannot
592 completely exclude that some other INs than $V1^R$ were affected by 4-AP application, but it is
593 important to note that $V1^R$ are the first INs contacting MNs and producing GABA at the onset

594 of the SNA in the embryonic SC [25], which makes them the best candidates to explain the
595 effect of 4-AP.

596 The relationship between the firing pattern and the amount of neurotransmitter release
597 could *a priori* explain why GIC amplitude strongly varied between SC preparation [12], the
598 proportion of the different firing patterns within the GABAergic $V1^R$ population likely
599 varying from one embryo to another at E12.5. However, that variability has little effect on
600 GDP amplitude. This can be explained by the depolarized equilibrium potential of chloride
601 ions at this developmental age (-30 mV) [82] and by the high input resistance of MNs, which
602 reduces the number of activated $GABA_A$ receptors needed for generating a GDP of maximal
603 amplitude. The current generated by $GABA_A$ receptor activation in MNs is probably larger
604 than necessary to achieve maximal GDP amplitude. Robustness of GABAergic GDP seems
605 thus related to redundant $GABA_A$ receptors. It must also be noted that most MNs cannot
606 sustain tonic firing in response to long lasting suprathreshold depolarization at E12.5. This
607 makes them poorly sensitive to fluctuations in GDP duration, as was experimentally observed.
608 This points out to another redundant process (the GDP duration is longer than required to
609 generate MN firing) involved in the robustness of SNA episodes. In addition, the degeneracy
610 of neurotransmitter systems that we previously observed (Czarnecki et al. 2014) also
611 contributes to the robustness of SNA. GDPs in MNs are evoked mainly by GABA release and,
612 to a lesser extent, by glutamate release. However, blocking either of these two
613 neurotransmitter systems alters neither the amplitude, nor the duration of the GDPs recorded
614 in MNs at E12.5 [12].

615

616 ***Conclusions.***

617 In conclusion, our results indicate that a single mechanism involving two classes of
618 voltage-gated channels with opposite functions is sufficient to produce functional diversity

619 between neurons and to account for the unusual developmental pattern of immature $V1^R$
620 during the important time window where SNA is expressed. To our knowledge, such a
621 mechanism was never described during embryonic development. Importantly, this
622 demonstrates that diversity of the electrical phenotype between neurons and robustness of a
623 given firing pattern does not necessitate the presence of many different classes of voltage-
624 gated channels.

625 Our results also reveal the robustness of GDPs in MNs during SNA at E12.5 MNs. It likely
626 results from several processes, including GABAergic receptor redundancy and
627 neurotransmitter degeneracy, that counterbalance the functional heterogeneity of INs. Such
628 mechanisms are likely of great importance during SC development since the robustness of
629 SNA pattern at a given age is required for correct MN axon pathfinding and establishment of
630 the first functional motor network [21, 23, 83].

631 ## Materials and Methods

632 ***Isolated spinal cord preparation.***

633 Experiments were performed in accordance with European Community guiding principles
634 on the care and use of animals (86/609/CEE, CE Off J no. L358, 18 December 1986), French
635 decree no. 97/748 of October 19, 1987 (J Off République Française, 20 October 1987, pp.
636 12245-12248). All procedures were carried out in accordance with the local ethics committee
637 of local Universities and recommendations from the CNRS. We used GAD67eGFP knock-in
638 mice to visualize putative GABAergic INs [84], as in our previous study (Boeri et al. 2018).
639 To obtain E12.5-E16.5 transgenic GAD67-eGFP embryos, 8 to 12 weeks old wild-type Swiss
640 female mice were crossed with GAD67-eGFP Swiss male mice.

641 Isolated mouse SCs from 420 embryos were used in this work and obtained as previously
642 described [82, 85]. Briefly, pregnant mice were anesthetized by intramuscular injection of a
643 mix of ketamine and xylazine and sacrificed using a lethal dose of CO_2 after embryos of
644 either sex were removed. Whole SCs were isolated from eGFP-positive embryos and
645 maintained in an artificial cerebrospinal fluid (ACSF) containing 135 mM NaCl, 25 mM
646 $NaHCO_3$, 1 mM NaH_2PO_4, 3 mM KCl, 11 mM glucose, 2 mM $CaCl_2$, and 1 mM $MgCl_2$ (307
647 mOsm/kg H_2O), continuously bubbled with a 95% O_2-5% CO_2 gas mixture.

648 In the lumbar SC of GAD67eGFP mouse embryos, eGFP neurons were detected using 488
649 nm UV light. They were localized in the ventro-lateral marginal zone between the motor
650 columns and the ventral funiculi [63]. Embryonic $V1^R$ identity was confirmed by the
651 expression of the forkhead transcription factor Foxd3 [25].

652

653 ***Whole-cell recordings and analysis.***

654 The isolated SC was placed in a recording chamber and was continuously perfused (2
655 ml/min) at room temperature (22-26°C) with oxygenated ACSF. Whole-cell patch-clamp

656 recordings of lumbar spinal embryonic $V1^R$ were carried out under direct visualization using
657 an infrared-sensitive CCD video camera. Whole-cell patch-clamp electrodes with a resistance
658 of 4-7 MΩ were pulled from thick-wall borosilicate glass using a P-97 horizontal puller
659 (Sutter Instrument Co., USA). They were filled with a solution containing (in mM): 96.4 K
660 methanesulfonate, 33.6 KCl, 4 $MgCl_2$, 4 Na_2ATP, 0.3 Na_3GTP, 10 EGTA, and 10 HEPES
661 (pH 7.2; 290 mOsm/kg-H_2O). This intracellular solution led to an equilibrium potential of
662 chloride ions, E_{Cl}, of about -30 mV, close to the physiological values measured at E12.5 in
663 spinal MNs [82]. The junction potential (6.6 mV) was systematically corrected offline.

664 Signals were recorded using Multiclamp 700B amplifiers (Molecular Devices, USA). Data
665 were low-pass filtered (2 kHz), digitized (20 kHz) online using Digidata 1440A or 1550B
666 interfaces and acquired using pCLAMP 10.5 software (Molecular Devices, USA). Analyses
667 were performed off-line using pCLAMP 10.5 and Axograph 1.7.2 (Molecular devices;
668 RRID:SCR_014284) software packages.

669 In voltage-clamp mode, voltage-dependent K^+ currents (I_{Kv}) were elicited by 500 ms
670 depolarizing voltage steps (10 mV increments, 10 s interval) after a prepulse of 300 ms at V_H
671 = -100 mV. To isolate the delayed rectifier potassium current I_{Kdr}, voltage steps were applied
672 after a 300 ms prepulse at V_H = -30 mV that inactivated the low threshold transient potassium
673 current I_A. I_A was then obtained by subtracting offline I_{Kdr} from the total potassium current
674 I_{Kv}. Capacitance and leak current were subtracted using on-line P/4 protocol provided by
675 pCLAMP 10.5.

676 In current-clamp mode, $V1^R$ discharge was elicited using 2 s depolarizing current steps
677 (from 0 to ≈ 50 pA in 5-10 pA increments, depending on the input resistance of the cell) with
678 an 8 s interval to ensure that the membrane potential returned to V_H. When a cell generated a
679 sustained discharge, the intensity of the depolarizing pulse was reduced to the minimal value
680 compatible with repetitive firing.

681 The persistent sodium current I_{Nap} was measured in voltage-clamp mode using a 70 mV/s
682 depolarizing voltage ramp [86]. This speed was slow enough to preclude substantial
683 contamination by the inactivating transient current and fast enough to avoid substantial
684 inactivation of I_{Nap}. Subtraction of the current evoked by the voltage ramp in the presence of
685 1 μM tetrodotoxin (TTX) from the control voltage ramp-evoked current revealed I_{Nap}.
686
687 ***Pharmacological reagents.***
688 During patch-clamp recordings, bath application of TTX (1 μM, Alomone, Israel) or 4-AP
689 (0.3 - 600 μM, Sigma) was done using 0.5 mm diameter quartz tubing positioned, under direct
690 visual control, 50 μm away from the recording area. The quartz tubing was connected to 6
691 solenoid valves linked with 6 reservoirs *via* a manifold. Solutions were gravity-fed into the
692 quartz tubing. Their application was controlled using a VC-8 valve controller (Warner
693 Instruments, USA).
694 4-aminopyridine (4-AP; Sigma Aldrich, USA) was used to block I_{Kdr}. To determine the
695 concentration–response curve, $I - V$ curves of I_{Kdr} for different concentrations of 4-AP (0.3
696 to 300 μM) were compared to the control curve obtained in the absence of 4-AP. The
697 percentage of inhibition for a given concentration was calculated by dividing the peak
698 intensity of I_{Kdr} by the peak value obtained in control condition. The obtained normalized
699 concentration–response curves were fitted using the Hill equation:
700 $\frac{100-I_{min}}{1+([4-AP]/IC_{50})^{n_H}} + I_{min}$,
701 where [4-AP] is the 4-AP concentration, I_{min} is the residual current (in percentage of the peak
702 I_{Kdr}), $100 - I_{min}$ is the maximal inhibition achieved for saturating concentration of 4-AP,
703 IC_{50} is the 4-AP concentration producing half of the maximal inhibition, and n_H is the Hill
704 coefficient. Curve fitting was performed using KaleidaGraph 4.5 (Synergy Software, USA).
705

706 ***Immunohistochemistry and confocal microscopy.***

707 E14.5 embryos were collected from pregnant females. Once dissected out of their yolk sac,
708 SCs were dissected and immediately immersion-fixed in phosphate buffer (PB 0.1 M)
709 containing 4% paraformaldehyde (PFA; freshly prepared in PB, pH 7.4) for 1 h at 4°C. Whole
710 SCs were then rinsed out in 0.12 M PB at 4°C, thawed at room temperature, washed in PBS,
711 incubated in NH_4Cl (50 mM), diluted in PBS for 20 min and then permeabilized for 30 min in
712 a blocking solution (10% goat serum in PBS) with 0.2% Triton X-100. They were incubated
713 for 48 h at 4°C in the presence of the following primary antibodies: guinea pig anti-FoxD3
714 (1:5000, gift from Carmen Birchmeier and Thomas Müller of the Max Delbrück Center for
715 Molecular Medicine in Berlin) and rabbit anti-cleaved Caspase-3 (1:1000, Cell Signaling
716 Technology Cat# 9661, RRID:AB_2341188). SCs were then washed in PBS and incubated
717 for 2 h at RT with secondary fluorescent antibodies (goat anti-rabbit-conjugated 649; donkey
718 anti-guinea pig-conjugated Alexa Fluor 405 [1:1000, ThermoFisher]) diluted in 0.2% Triton
719 X-100 blocking solution. After washing in PBS, SCs were dried and mounted in Mowiol
720 medium (Millipore, Molsheim, France). Preparations were then imaged using a Leica SP5
721 confocal microscope. Immunostaining was observed using a 40X oil-immersion objective
722 with a numerical aperture of 1.25, as well as with a 63X oil-immersion objective with a
723 numerical aperture of 1.32. Serial optical sections were obtained with a Z-step of 1 µm (40X)
724 and 0.2-0.3 µm (63X). Images (1024x1024; 12-bit color scale) were stored using Leica
725 software LAS-AF and analyzed using ImageJ 1.5 (N.I.H., USA; http//rsb.info.nih.gov/ij/) and
726 Adobe Photoshop CS6 (Adobe, USA) software.

727

728 ***Cluster analysis.***

729 To classify the firing patterns of embryonic $V1^R$, we performed a hierarchical cluster
730 analysis on a population of 163 cells. Each cell was characterized by three quantitative

731 measures of its firing pattern (see legend of Fig 1). After normalizing these quantities to zero
732 mean and unit variance, we performed a hierarchical cluster analysis using the hclust function
733 in R software (version 3.3.2, https://cran.r-project.org/) that implements the complete linkage
734 method. The intercluster distance was defined as the maximum Euclidean distance between
735 the points of two clusters, and, at each step of the process, the two closest clusters were
736 merged into a single one, thus constructing progressively a dendrogram. Clusters were then
737 displayed in data space using the dendromat function in the R package 'squash' dedicated to
738 color-based visualization of multivariate data. The best clustering was determined using the
739 silhouette measure of clustering consistency [87]. The silhouette of a data point, based on the
740 comparison of its distance to other points in the same cluster and to points in the closest
741 cluster, ranges from -1 to 1. A value near 1 indicates that the point is well assigned to its
742 cluster, a value near 0 indicates that it is close to the decision boundary between two
743 neighboring clusters, and negative values may indicate incorrect assignment to the cluster.
744 This allowed us to identify an optimal number k of clusters by maximizing the overall
745 average silhouette over a range of possible values for k [87], using the silhouette function in
746 the R package 'cluster'.
747
748 ***Biophysical modeling.***
749 To understand the relationship between the voltage-dependent membrane conductances
750 and the firing patterns of embryonic $V1^R$, we relied on a single compartment conductance
751 based model that included the leak current, the transient and persistent components of the
752 sodium current, I_{Nat} and I_{Nap}, and a delayed rectifier potassium current I_{Kdr}. Voltage
753 evolution then followed the equation
754 $C_{in}\frac{dV}{dt} = G_{in}(V_H - V) + G_{Nat}m^3h(E_{Na} - V) + G_{Nap}m_p^3(E_{Na} - V) + G_{Kdr}n^3(E_K - V) + I$ (1),

755 where C_{in} was the input capacitance; G_{in} the input conductance; G_{Nat}, G_{Nap}, G_{Kdr} the
756 maximal conductances of the aforementioned currents; m, m_p and n their activation variables;
757 h the inactivation variable of I_{Nat}; V_H the baseline potential imposed by *ad hoc* current
758 injection in current-clamp experiments; E_{Na} and E_K the Nernst potentials of sodium and
759 potassium ions, and I the injected current. All gating variables satisfied equations of the form:

760 $$\tau_x \frac{dx}{dt} = x_\infty(V) - x,$$

761 where the (in)activation curves were sigmoid functions of the form:

762 $$x_\infty = \frac{1}{1+\exp\left(-(V-V_{x)}/k_x\right)}$$

763 with k_x being positive for activation and negative for inactivation. The time constant τ_x was
764 voltage-independent except for the inactivation variable h.

765 To take into account the inactivating potassium current I_A revealed by experiments, we
766 also considered a model with the additional term $G_A m_A h_A (E_K - V)$ added to the right-hand-
767 side of equation (1). The activation variable m_A of I_A was assumed to follow any voltage
768 change instantaneously while its inactivation variable evolved more slowly.

769 To explain the more complex activity patterns observed in 27 % of the cells, we added a
770 slow inactivation variable s to I_{Nap}, which became $G_{Nap} m_p^3 s (V_{Na} - V)$. We considered that
771 the corresponding time constant τ_s could be voltage-dependent.

772 The effect of channel noise was investigated with a stochastic realization of the model,
773 where channels kinetics were described by Markov-type models, assuming a unitary channel
774 conductance of 10 pS for all channels.

775 Most model parameters were chosen on the basis of experimental measurements (see S1
776 File). Parameters that could not be constrained from our experimental data were chosen from
777 an experimentally realistic range of values.

778

779 ***Numerical simulations and dynamical systems analysis.***

780 We integrated numerically the deterministic model using the freeware XPPAUT [88] and a
781 standard fourth-order Runge-Kutta algorithm. XPPAUT was also used to compute one-
782 parameter and two-parameters bifurcation diagrams. The stochastic version of the model was
783 also implemented in XPPAUT and computed with a Gillespie's algorithm [89].

784 To investigate the dynamics of the model with slow inactivation of I_{Nap}, we relied on
785 numerical simulations together with fast/slow dynamics analysis [90]. In this approach, one
786 distinguishes slow dynamical variables (here only s) and fast dynamical variables. Slow
787 variables vary little at the time scale of fast variables and may therefore be considered as
788 constant parameters of the fast dynamics in first approximation. In contrast, slow variables are
789 essentially sensitive to the time average of the fast variables, much more than to their
790 instantaneous values. This separation of time scales allows one to conduct a phase plane
791 analysis of the full dynamics.

792

793 ***Statistics.***

794 All values were expressed as mean ± SEM. Statistical significance was assessed by non-
795 parametric Kruskal-Wallis test with Dunn's post hoc test, Mann-Whitney test or Wilcoxon
796 matched pairs test (GraphPad Prism 5.0 Software, USA). Significant changes in the
797 proportions of firing patterns with age were assessed by chi-square test for large sample and
798 by Fisher's exact test for small sample. Significance was determined at $P < 0.05$.

Acknowledgments

We thank Susanne Bolte, Jean-François Gilles and Richard Schwartzmann for assistance with confocal imaging (IBPS imaging facility) and IBPS rodent facility team for animal care and production. We thank University Paris Descartes for hosting Yulia Timofeeva as an invited professor. This work was supported by INSERM, CNRS, Sorbonne Université (Paris), Université de Bordeaux, Université Paris Descartes and Fondation pour la Recherche Médicale.

806 **References**

807 1. O'Donovan MJ. The origin of spontaneous activity in developing networks of the
808 vertebrate nervous system. Curr Opin Neurobiol. 1999;9(1):94-104. PubMed PMID:
809 10072366.
810 2. Saint-Amant L. Development of motor rhythms in zebrafish embryos. Progress in brain
811 research. 2010;187:47-61. doi: 10.1016/B978-0-444-53613-6.00004-6. PubMed PMID:
812 21111200.
813 3. Blankenship AG, Feller MB. Mechanisms underlying spontaneous patterned activity in
814 developing neural circuits. Nature reviews Neuroscience. 2010;11(1):18-29. doi:
815 10.1038/nrn2759. PubMed PMID: 19953103; PubMed Central PMCID: PMC2902252.
816 4. Myers CP, Lewcock JW, Hanson MG, Gosgnach S, Aimone JB, Gage FH, et al.
817 Cholinergic input is required during embryonic development to mediate proper
818 assembly of spinal locomotor circuits. Neuron. 2005;46(1):37-49. Epub 2005/04/12. doi:
819 S0896-6273(05)00165-0 [pii] 10.1016/j.neuron.2005.02.022. PubMed PMID: 15820692.
820 5. Milner LD, Landmesser LT. Cholinergic and GABAergic inputs drive patterned
821 spontaneous motoneuron activity before target contact. J Neurosci. 1999;19(8):3007-22.
822 PubMed PMID: 10191318.
823 6. Hanson MG, Landmesser LT. Characterization of the circuits that generate spontaneous
824 episodes of activity in the early embryonic mouse spinal cord. J Neurosci.
825 2003;23(2):587-600. PubMed PMID: 12533619.
826 7. Momose-Sato Y, Sato K. Large-scale synchronized activity in the embryonic brainstem
827 and spinal cord. Frontiers in cellular neuroscience. 2013;7:36. doi:
828 10.3389/fncel.2013.00036. PubMed PMID: 23596392; PubMed Central PMCID:
829 PMC3625830.
830 8. Khazipov R, Luhmann HJ. Early patterns of electrical activity in the developing
831 cerebral cortex of humans and rodents. Trends in neurosciences. 2006;29(7):414-8. doi:
832 10.1016/j.tins.2006.05.007. PubMed PMID: 16713634.
833 9. Allain AE, Le Corronc H, Delpy A, Cazenave W, Meyrand P, Legendre P, et al.
834 Maturation of the GABAergic transmission in normal and pathologic motoneurons.
835 Neural plasticity. 2011;2011:905624. doi: 10.1155/2011/905624. PubMed PMID:
836 21785735; PubMed Central PMCID: PMC3140191.
837 10. Branchereau P, Chapron J, Meyrand P. Descending 5-hydroxytryptamine raphe inputs
838 repress the expression of serotonergic neurons and slow the maturation of inhibitory

839 systems in mouse embryonic spinal cord. J Neurosci. 2002;22(7):2598-606. doi:
840 20026199. PubMed PMID: 11923425.
841 11. Yvert B, Branchereau P, Meyrand P. Multiple spontaneous rhythmic activity patterns
842 generated by the embryonic mouse spinal cord occur within a specific developmental
843 time window. Journal of neurophysiology. 2004;91(5):2101-9. doi:
844 10.1152/jn.01095.2003. PubMed PMID: 14724265.
845 12. Czarnecki A, Le Corronc H, Rigato C, Le Bras B, Couraud F, Scain AL, et al.
846 Acetylcholine controls GABA-, glutamate-, and glycine-dependent giant depolarizing
847 potentials that govern spontaneous motoneuron activity at the onset of synaptogenesis in
848 the mouse embryonic spinal cord. J Neurosci. 2014;34(18):6389-404. doi:
849 10.1523/JNEUROSCI.2664-13.2014. PubMed PMID: 24790209.
850 13. Pun S, Sigrist M, Santos AF, Ruegg MA, Sanes JR, Jessell TM, et al. An intrinsic
851 distinction in neuromuscular junction assembly and maintenance in different skeletal
852 muscles. Neuron. 2002;34(3):357-70. doi: 10.1016/s0896-6273(02)00670-0. PubMed
853 PMID: 11988168.
854 14. Angelim M, Maia L, Mouffle C, Ginhoux F, Low D, Amancio-Dos-Santos A, et al.
855 Embryonic macrophages and microglia ablation alter the development of dorsal root
856 ganglion sensory neurons in mouse embryos. Glia. 2018;66(11):2470-86. doi:
857 10.1002/glia.23499. PubMed PMID: 30252950.
858 15. Marmigere F, Ernfors P. Specification and connectivity of neuronal subtypes in the
859 sensory lineage. Nature reviews Neuroscience. 2007;8(2):114-27. doi: 10.1038/nrn2057.
860 PubMed PMID: 17237804.
861 16. Ozaki S, Snider WD. Initial trajectories of sensory axons toward laminar targets in the
862 developing mouse spinal cord. The Journal of comparative neurology. 1997;380(2):215-
863 29. PubMed PMID: 9100133.
864 17. Ballion B, Branchereau P, Chapron J, Viala D. Ontogeny of descending serotonergic
865 innervation and evidence for intraspinal 5-HT neurons in the mouse spinal cord. Brain
866 research Developmental brain research. 2002;137(1):81-8. doi: 10.1016/s0165-
867 3806(02)00414-5. PubMed PMID: 12128257.
868 18. Moody WJ, Bosma MM. Ion channel development, spontaneous activity, and activity-
869 dependent development in nerve and muscle cells. Physiological reviews.
870 2005;85(3):883-941. doi: 10.1152/physrev.00017.2004. PubMed PMID: 15987798.
871 19. Spitzer NC. Electrical activity in early neuronal development. Nature.
872 2006;444(7120):707-12. doi: 10.1038/nature05300. PubMed PMID: 17151658.

873 20. Katz LC, Shatz CJ. Synaptic activity and the construction of cortical circuits. Science.
874 1996;274(5290):1133-8. PubMed PMID: 8895456.
875 21. Hanson MG, Milner LD, Landmesser LT. Spontaneous rhythmic activity in early
876 chick spinal cord influences distinct motor axon pathfinding decisions. Brain Res Rev.
877 2008;57(1):77-85. Epub 2007/10/09. doi: S0165-0173(07)00127-0 [pii]
878 10.1016/j.brainresrev.2007.06.021. PubMed PMID: 17920131.
879 22. Hanson MG, Landmesser LT. Normal patterns of spontaneous activity are required for
880 correct motor axon guidance and the expression of specific guidance molecules. Neuron.
881 2004;43(5):687-701. doi: 10.1016/j.neuron.2004.08.018. PubMed PMID: 15339650.
882 23. Hanson MG, Landmesser LT. Increasing the frequency of spontaneous rhythmic
883 activity disrupts pool-specific axon fasciculation and pathfinding of embryonic spinal
884 motoneurons. J Neurosci. 2006;26(49):12769-80. doi: 10.1523/JNEUROSCI.4170-
885 06.2006. PubMed PMID: 17151280.
886 24. Benito-Gonzalez A, Alvarez FJ. Renshaw cells and Ia inhibitory interneurons are
887 generated at different times from p1 progenitors and differentiate shortly after exiting
888 the cell cycle. J Neurosci. 2012;32(4):1156-70. doi: 10.1523/JNEUROSCI.3630-
889 12.2012. PubMed PMID: 22279202; PubMed Central PMCID: PMC3276112.
890 25. Boeri J, Le Corronc H, Lejeune FX, Le Bras B, Mouffle C, Angelim M, et al.
891 Persistent Sodium Current Drives Excitability of Immature Renshaw Cells in Early
892 Embryonic Spinal Networks. J Neurosci. 2018;38(35):7667-82. doi:
893 10.1523/JNEUROSCI.3203-17.2018. PubMed PMID: 30012693.
894 26. Perry S, Gezelius H, Larhammar M, Hilscher MM, Lamotte d'Incamps B, Leao KE, et
895 al. Firing properties of Renshaw cells defined by Chrna2 are modulated by
896 hyperpolarizing and small conductance ion currents Ih and ISK. The European journal
897 of neuroscience. 2015;41(7):889-900. doi: 10.1111/ejn.12852. PubMed PMID:
898 25712471.
899 27. Bikoff JB, Gabitto MI, Rivard AF, Drobac E, Machado TA, Miri A, et al. Spinal
900 Inhibitory Interneuron Diversity Delineates Variant Motor Microcircuits. Cell.
901 2016;165(1):207-19. doi: 10.1016/j.cell.2016.01.027. PubMed PMID: 26949184;
902 PubMed Central PMCID: PMC4808435.
903 28. Sillar KT, Simmers AJ, Wedderburn JF. The post-embryonic development of cell
904 properties and synaptic drive underlying locomotor rhythm generation in Xenopus
905 larvae. Proceedings Biological sciences. 1992;249(1324):65-70. doi:
906 10.1098/rspb.1992.0084. PubMed PMID: 1359549.

907 29. Gao BX, Ziskind-Conhaim L. Development of ionic currents underlying changes in
908 action potential waveforms in rat spinal motoneurons. Journal of neurophysiology.
909 1998;80(6):3047-61. PubMed PMID: 9862905.
910 30. Gao H, Lu Y. Early development of intrinsic and synaptic properties of chicken
911 nucleus laminaris neurons. Neuroscience. 2008;153(1):131-43. doi:
912 10.1016/j.neuroscience.2008.01.059. PubMed PMID: 18355968.
913 31. McKay BE, Turner RW. Physiological and morphological development of the rat
914 cerebellar Purkinje cell. J Physiol. 2005;567(Pt 3):829-50. doi:
915 10.1113/jphysiol.2005.089383. PubMed PMID: 16002452; PubMed Central PMCID:
916 PMC1474219.
917 32. Liu X, Pfaff DW, Calderon DP, Tabansky I, Wang X, Wang Y, et al. Development of
918 Electrophysiological Properties of Nucleus Gigantocellularis Neurons Correlated with
919 Increased CNS Arousal. Developmental neuroscience. 2016;38(4):295-310. doi:
920 10.1159/000449035. PubMed PMID: 27788521; PubMed Central PMCID:
921 PMC5127753.
922 33. Pineda R, Ribera A. Evolution of the Action Potential. In: Kaas JH, editor. Evolution
923 of Nervous Systems. 1: Elsevier Ltd; 2010. p. 211-38.
924 34. Crill WE. Persistent sodium current in mammalian central neurons. Annual review of
925 physiology. 1996;58:349-62. doi: 10.1146/annurev.ph.58.030196.002025. PubMed
926 PMID: 8815799.
927 35. Sigworth FJ, Sine SM. Data transformations for improved display and fitting of
928 single-channel dwell time histograms. Biophysical journal. 1987;52(6):1047-54. doi:
929 10.1016/S0006-3495(87)83298-8. PubMed PMID: 2447968; PubMed Central PMCID:
930 PMC1330104.
931 36. Ramoa AS, McCormick DA. Developmental changes in electrophysiological
932 properties of LGNd neurons during reorganization of retinogeniculate connections. J
933 Neurosci. 1994;14(4):2089-97. PubMed PMID: 8158259; PubMed Central PMCID:
934 PMC6577110.
935 37. Belleau ML, Warren RA. Postnatal development of electrophysiological properties of
936 nucleus accumbens neurons. Journal of neurophysiology. 2000;84(5):2204-16. doi:
937 10.1152/jn.2000.84.5.2204. PubMed PMID: 11067966.
938 38. Picken Bahrey HL, Moody WJ. Early development of voltage-gated ion currents and
939 firing properties in neurons of the mouse cerebral cortex. Journal of neurophysiology.
940 2003;89(4):1761-73. doi: 10.1152/jn.00972.2002. PubMed PMID: 12611962.

941 39. Tong H, McDearmid JR. Pacemaker and plateau potentials shape output of a
942 developing locomotor network. Current biology : CB. 2012;22(24):2285-93. doi:
943 10.1016/j.cub.2012.10.025. PubMed PMID: 23142042; PubMed Central PMCID:
944 PMC3525839.
945 40. Alvarez FJ, Benito-Gonzalez A, Siembab VC. Principles of interneuron development
946 learned from Renshaw cells and the motoneuron recurrent inhibitory circuit. Annals of
947 the New York Academy of Sciences. 2013;1279:22-31. doi: 10.1111/nyas.12084.
948 PubMed PMID: 23530999; PubMed Central PMCID: PMC3870136.
949 41. Allain AE, Segu L, Meyrand P, Branchereau P. Serotonin controls the maturation of
950 the GABA phenotype in the ventral spinal cord via 5-HT1b receptors. Annals of the
951 New York Academy of Sciences. 2010;1198:208-19. doi: 10.1111/j.1749-
952 6632.2010.05433.x. PubMed PMID: 20536936.
953 42. Branchereau P, Morin D, Bonnot A, Ballion B, Chapron J, Viala D. Development of
954 lumbar rhythmic networks: from embryonic to neonate locomotor-like patterns in the
955 mouse. Brain research bulletin. 2000;53(5):711-8. doi: 10.1016/s0361-9230(00)00403-2.
956 PubMed PMID: 11165805.
957 43. Spitzer NC, Vincent A, Lautermilch NJ. Differentiation of electrical excitability in
958 motoneurons. Brain research bulletin. 2000;53(5):547-52. PubMed PMID: 11165790.
959 44. Prasad T, Wang X, Gray PA, Weiner JA. A differential developmental pattern of
960 spinal interneuron apoptosis during synaptogenesis: insights from genetic analyses of
961 the protocadherin-gamma gene cluster. Development. 2008;135(24):4153-64. doi:
962 10.1242/dev.026807. PubMed PMID: 19029045; PubMed Central PMCID:
963 PMC2755264.
964 45. Coetzee WA, Amarillo Y, Chiu J, Chow A, Lau D, McCormack T, et al. Molecular
965 diversity of K+ channels. Annals of the New York Academy of Sciences.
966 1999;868:233-85. doi: 10.1111/j.1749-6632.1999.tb11293.x. PubMed PMID: 10414301.
967 46. Gutman GA, Chandy KG, Grissmer S, Lazdunski M, McKinnon D, Pardo LA, et al.
968 International Union of Pharmacology. LIII. Nomenclature and molecular relationships
969 of voltage-gated potassium channels. Pharmacological reviews. 2005;57(4):473-508.
970 doi: 10.1124/pr.57.4.10. PubMed PMID: 16382104.
971 47. Liu SJ, Kaczmarek LK. The expression of two splice variants of the Kv3.1 potassium
972 channel gene is regulated by different signaling pathways. J Neurosci. 1998;18(8):2881-
973 90. PubMed PMID: 9526005; PubMed Central PMCID: PMC6792597.

48. Song ZM, Hu J, Rudy B, Redman SJ. Developmental changes in the expression of calbindin and potassium-channel subunits Kv3.1b and Kv3.2 in mouse Renshaw cells. Neuroscience. 2006;139(2):531-8. doi: 10.1016/j.neuroscience.2005.12.048. PubMed PMID: 16460880.
49. Taddese A, Bean BP. Subthreshold sodium current from rapidly inactivating sodium channels drives spontaneous firing of tuberomammillary neurons. Neuron. 2002;33(4):587-600. doi: 10.1016/s0896-6273(02)00574-3. PubMed PMID: 11856532.
50. Kuo JJ, Lee RH, Zhang L, Heckman CJ. Essential role of the persistent sodium current in spike initiation during slowly rising inputs in mouse spinal neurones. J Physiol. 2006;574(Pt 3):819-34. doi: 10.1113/jphysiol.2006.107094. PubMed PMID: 16728453; PubMed Central PMCID: PMC1817738.
51. Teka W, Tsaneva-Atanasova K, Bertram R, Tabak J. From plateau to pseudo-plateau bursting: making the transition. Bulletin of mathematical biology. 2011;73(6):1292-311. doi: 10.1007/s11538-010-9559-7. PubMed PMID: 20658200; PubMed Central PMCID: PMC3152987.
52. Bertram R, Butte MJ, Kiemel T, Sherman A. Topological and phenomenological classification of bursting oscillations. Bulletin of mathematical biology. 1995;57(3):413-39. doi: 10.1007/BF02460633. PubMed PMID: 7728115.
53. Izhikevich EM. Neural excitability, spiking and bursting. Int J Bifurcation Chaos. 2000;10(06):1171-266.
54. Borisyuk A, Rinzel J. Understanding neuronal dynamics by geometrical dissection of minimal models. In: Chow C, Gutkin B, Hansel D, Meunier C, Dalibard J, editors. Models and Methods in Neurophysics. Proc Les Houches Summer School 2003, (Session LXXX): Elsevier; 2005. p. 19-72.
55. Rinzel J. Bursting oscillations in an excitable membrane model. In: Sleeman B, Jarvis R, editors. Ordinary and Partial Differential Equations Lecture Notes in Mathematics. 1151. Berlin, Heidelberg: Springer; 1985. p. 304–16.
56. Stern JV, Osinga HM, LeBeau A, Sherman A. Resetting behavior in a model of bursting in secretory pituitary cells: distinguishing plateaus from pseudo-plateaus. Bulletin of mathematical biology. 2008;70(1):68-88. doi: 10.1007/s11538-007-9241-x. PubMed PMID: 17703340.
57. Osinga HM, Tsaneva-Atanasova KT. Dynamics of plateau bursting depending on the location of its equilibrium. Journal of neuroendocrinology. 2010;22(12):1301-14. doi: 10.1111/j.1365-2826.2010.02083.x. PubMed PMID: 20955345.

58. Osinga HM, Sherman A, Tsaneva-Atanasova K. Cross-Currents between Biology and Mathematics: The Codimension of Pseudo-Plateau Bursting. Discrete and continuous dynamical systems Series A. 2012;32(8):2853-77. doi: 10.3934/dcds.2012.32.2853. PubMed PMID: 22984340; PubMed Central PMCID: PMC3439852.
59. Izhikevich EM. Subcritical Elliptic Bursting of Bautin Type. SIAM Journal on Applied Mathematics. 2000;60(2):503-35. doi: https://doi.org/10.1137/S003613999833263X.
60. Su J, Rubin J, Terman D. Effects of noise on elliptic bursters. Nonlinearity. 2004;17(1):133-57. doi: https://doi.org/10.1088/0951-7715/17/1/009.
61. Baer SM, Erneux T, Rinzel J. The Slow Passage through a Hopf Bifurcation: Delay, Memory Effects, and Resonance. SIAM Journal on Applied Mathematics. 1989;49(1):55-71. doi: https://doi.org/10.1137/0149003.
62. Holden S, Erneux T. Slow Passage Through a Hopf Bifurcation: From Oscillatory to Steady State Solutions. SIAM Journal on Applied Mathematics. 1993;53(4):1045-58. doi: https://doi.org/10.1137/0153052.
63. Stam FJ, Hendricks TJ, Zhang J, Geiman EJ, Francius C, Labosky PA, et al. Renshaw cell interneuron specialization is controlled by a temporally restricted transcription factor program. Development. 2012;139(1):179-90. doi: 10.1242/dev.071134. PubMed PMID: 22115757; PubMed Central PMCID: PMC3231776.
64. Eccles JC, Fatt P, Landgren S. The inhibitory pathway to motoneurones. Progress in neurobiology. 1956;(2):72-82. PubMed PMID: 13441782.
65. Hao MM, Lomax AE, McKeown SJ, Reid CA, Young HM, Bornstein JC. Early development of electrical excitability in the mouse enteric nervous system. J Neurosci. 2012;32(32):10949-60. doi: 10.1523/JNEUROSCI.1426-12.2012. PubMed PMID: 22875929; PubMed Central PMCID: PMC6621017.
66. Vinay L, Brocard F, Clarac F. Differential maturation of motoneurons innervating ankle flexor and extensor muscles in the neonatal rat. The European journal of neuroscience. 2000;12(12):4562-6. doi: 10.1046/j.0953-816x.2000.01321.x. PubMed PMID: 11122369.
67. Durand J, Filipchuk A, Pambo-Pambo A, Amendola J, Borisovna Kulagina I, Gueritaud JP. Developing electrical properties of postnatal mouse lumbar motoneurons. Frontiers in cellular neuroscience. 2015;9:349. doi: 10.3389/fncel.2015.00349. PubMed PMID: 26388736; PubMed Central PMCID: PMC4557103.

1041 68. Drion G, O'Leary T, Marder E. Ion channel degeneracy enables robust and tunable
1042 neuronal firing rates. Proceedings of the National Academy of Sciences of the United
1043 States of America. 2015;112(38):E5361-70. doi: 10.1073/pnas.1516400112. PubMed
1044 PMID: 26354124; PubMed Central PMCID: PMC4586887.
1045 69. Marcotti W, Johnson SL, Holley MC, Kros CJ. Developmental changes in the
1046 expression of potassium currents of embryonic, neonatal and mature mouse inner hair
1047 cells. J Physiol. 2003;548(Pt 2):383-400. doi: 10.1113/jphysiol.2002.034801. PubMed
1048 PMID: 12588897; PubMed Central PMCID: PMC2342842.
1049 70. Marcotti W, Johnson SL, Rusch A, Kros CJ. Sodium and calcium currents shape
1050 action potentials in immature mouse inner hair cells. J Physiol. 2003;552(Pt 3):743-61.
1051 doi: 10.1113/jphysiol.2003.043612. PubMed PMID: 12937295; PubMed Central
1052 PMCID: PMC2343463.
1053 71. Sontheimer H, Trotter J, Schachner M, Kettenmann H. Channel expression correlates
1054 with differentiation stage during the development of oligodendrocytes from their
1055 precursor cells in culture. Neuron. 1989;2(2):1135-45. doi: 10.1016/0896-
1056 6273(89)90180-3. PubMed PMID: 2560386.
1057 72. Allain AE, Bairi A, Meyrand P, Branchereau P. Ontogenic changes of the GABAergic
1058 system in the embryonic mouse spinal cord. Brain research. 2004;1000(1-2):134-47. doi:
1059 10.1016/j.brainres.2003.11.071. PubMed PMID: 15053961.
1060 73. Sapir T, Geiman EJ, Wang Z, Velasquez T, Mitsui S, Yoshihara Y, et al. Pax6 and
1061 engrailed 1 regulate two distinct aspects of renshaw cell development. J Neurosci.
1062 2004;24(5):1255-64. doi: 10.1523/JNEUROSCI.3187-03.2004. PubMed PMID:
1063 14762144; PubMed Central PMCID: PMC2997484.
1064 74. Henley J, Poo MM. Guiding neuronal growth cones using Ca2+ signals. Trends in cell
1065 biology. 2004;14(6):320-30. doi: 10.1016/j.tcb.2004.04.006. PubMed PMID: 15183189;
1066 PubMed Central PMCID: PMC3115711.
1067 75. Tsaneva-Atanasova K, Osinga HM, Riess T, Sherman A. Full system bifurcation
1068 analysis of endocrine bursting models. Journal of theoretical biology.
1069 2010;264(4):1133-46. doi: 10.1016/j.jtbi.2010.03.030. PubMed PMID: 20307553;
1070 PubMed Central PMCID: PMC3128456.
1071 76. Tagliavini A, Tabak J, Bertram R, Pedersen MG. Is bursting more effective than
1072 spiking in evoking pituitary hormone secretion? A spatiotemporal simulation study of
1073 calcium and granule dynamics. American journal of physiology Endocrinology and

1074 metabolism. 2016;310(7):E515-25. doi: 10.1152/ajpendo.00500.2015. PubMed PMID:
1075 26786781.
1076 77. Oster A, Faure P, Gutkin BS. Mechanisms for multiple activity modes of VTA
1077 dopamine neurons. Frontiers in computational neuroscience. 2015;9:95. doi:
1078 10.3389/fncom.2015.00095. PubMed PMID: 26283955; PubMed Central PMCID:
1079 PMC4516885.
1080 78. Chevalier M, Toporikova N, Simmers J, Thoby-Brisson M. Development of
1081 pacemaker properties and rhythmogenic mechanisms in the mouse embryonic
1082 respiratory network. eLife. 2016;5. doi: 10.7554/eLife.16125. PubMed PMID:
1083 27434668; PubMed Central PMCID: PMC4990420.
1084 79. Wang LY, Kaczmarek LK. High-frequency firing helps replenish the readily
1085 releasable pool of synaptic vesicles. Nature. 1998;394(6691):384-8. doi: 10.1038/28645.
1086 PubMed PMID: 9690475.
1087 80. Tibbs GR, Barrie AP, Van Mieghem FJ, McMahon HT, Nicholls DG. Repetitive
1088 action potentials in isolated nerve terminals in the presence of 4-aminopyridine: effects
1089 on cytosolic free Ca2+ and glutamate release. Journal of neurochemistry.
1090 1989;53(6):1693-9. doi: 10.1111/j.1471-4159.1989.tb09232.x. PubMed PMID:
1091 2553862.
1092 81. Hallermann S, Silver RA. Sustaining rapid vesicular release at active zones: potential
1093 roles for vesicle tethering. Trends in neurosciences. 2013;36(3):185-94. doi:
1094 10.1016/j.tins.2012.10.001. PubMed PMID: 23164531; PubMed Central PMCID:
1095 PMC4748400.
1096 82. Delpy A, Allain AE, Meyrand P, Branchereau P. NKCC1 cotransporter inactivation
1097 underlies embryonic development of chloride-mediated inhibition in mouse spinal
1098 motoneuron. J Physiol. 2008;586(4):1059-75. doi: 10.1113/jphysiol.2007.146993.
1099 PubMed PMID: 18096599; PubMed Central PMCID: PMC2375629.
1100 83. Kastanenka KV, Landmesser LT. In vivo activation of channelrhodopsin-2 reveals that
1101 normal patterns of spontaneous activity are required for motoneuron guidance and
1102 maintenance of guidance molecules. J Neurosci. 2010;30(31):10575-85. doi:
1103 10.1523/JNEUROSCI.2773-10.2010. PubMed PMID: 20686000; PubMed Central
1104 PMCID: PMC2934783.
1105 84. Tamamaki N, Yanagawa Y, Tomioka R, Miyazaki J, Obata K, Kaneko T. Green
1106 fluorescent protein expression and colocalization with calretinin, parvalbumin, and

somatostatin in the GAD67-GFP knock-in mouse. The Journal of comparative neurology. 2003;467(1):60-79. doi: 10.1002/cne.10905. PubMed PMID: 14574680.

85. Scain AL, Le Corronc H, Allain AE, Muller E, Rigo JM, Meyrand P, et al. Glycine release from radial cells modulates the spontaneous activity and its propagation during early spinal cord development. J Neurosci. 2010;30(1):390-403. Epub 2010/01/08. doi: 30/1/390 [pii] 10.1523/JNEUROSCI.2115-09.2010. PubMed PMID: 20053920.

86. Huang H, Trussell LO. Control of presynaptic function by a persistent Na(+) current. Neuron. 2008;60(6):975-9. doi: 10.1016/j.neuron.2008.10.052. PubMed PMID: 19109905; PubMed Central PMCID: PMC2657474.

87. Rousseeuw PJ. Silhouettes - a Graphical Aid to the Interpretation and Validation of Cluster-Analysis. J Comput Appl Math. 1987;20:53-65. doi: Doi 10.1016/0377-0427(87)90125-7. PubMed PMID: WOS:A1987L111800005.

88. Ermentrout B. Simulating, Analyzing, and Animating Dynamical Systems: A Guide to XPPAUT for Researchers and Students. Philadelphia: Society for Industrial and Applied Mathematics; 2002.

89. Gillespie DT. A general method for numerically simulating the stochastic time evolution of coupled chemical reactions. Journal of Computational Physics. 1976;22(4):403-34. doi: https://doi.org/10.1016/0021-9991(76)90041-3.

90. Witelski T, Bowen M. Fast/slow Dynamical Systems. In: Methods of Mathematical Modelling: Springer, Cham; 2015.

91. Rigato C, Buckinx R, Le-Corronc H, Rigo JM, Legendre P. Pattern of invasion of the embryonic mouse spinal cord by microglial cells at the time of the onset of functional neuronal networks. Glia. 2011;59(4):675-95. doi: 10.1002/glia.21140. PubMed PMID: 21305616.

1134 ## Figure captions

1135 **Fig 1. Cluster analysis of embryonic $V1^R$ firing pattern in the embryonic spinal cord at**
1136 **E12.5.**

1137 A inserts. Cluster analysis of embryonic $V1^R$ firing pattern was performed using three
1138 parameters that describe the firing pattern during a 2 s suprathreshold depolarizing pulses: the
1139 mean of the half-amplitude event duration (mean ½Ad), the coefficient of variation of ½ Ad
1140 (CV ½Ad) allowing to quantify the AP variation within a train (CV was set to 0 when the
1141 number of spikes evoked by a depolarizing pulse was ≤ 3) and the duration ratio ddr = Σ½
1142 Ad/Pw, obtained by dividing the sum of ½ Ad by the pulse duration Pw, that indicates the
1143 total time spent in the depolarized state. For example, ddr = 1 when a plateau potential lasts as
1144 long as the depolarizing pulse. Conversely, its value is low when the depolarizing pulse
1145 evokes a single AP only. A. Dendrogram for complete linkage hierarchical clustering of 163
1146 embryonic $V1^R$ according to the values of log mean ½Ad, of CV ½Ad and of log ddr. The
1147 colored matrix below the dendrogram shows the variations of these three parameters for all
1148 the cells in the clusters (colored trees) extracted from the dendrogram. B. The number of
1149 clusters was determined by analyzing the distribution of silhouette width values (see Material
1150 and Methods). The boxplots show the distribution of silhouette width values when the number
1151 of clusters k varies from 2 to 12. The mean silhouette width values (red diamond shaped
1152 points) attained their maximum when the estimated cluster number was 5. C. 3D plot showing
1153 cluster distribution of embryonic $V1^R$ according to log mean ½Ad, CV ½Ad and log ddr.
1154 Each cluster corresponds to a particular firing pattern as illustrated in D: $V1^R$ that cannot
1155 sustain repetitive firing of APs (1 to 3 AP/pulse only, gray), $V1^R$ that can fire tonically (red),
1156 $V1^R$ with a firing pattern characterized by a mix of APs and relatively short plateau potentials
1157 (dark purple), $V1^R$ with a firing pattern characterized by a mix of APs and relatively long
1158 plateau potentials (light purple) and $V1^R$ with evoked plateau potentials only (blue). The

1159 arrow in D indicates 3 misclassified $V1^R$ that could not sustain repetitive firing although they
1160 were assigned to the cluster of repetitively firing $V1^R$ (see text).
1161
1162 **Fig 2. Changes in the input capacitance, the input resistance and the threshold values of**
1163 **embryonic $V1^R$ from E11.5 to E16.5.**
1164 A. Graph showing how the input capacitance C_{in} of $V1^R$ changes with embryonic age. C_{in}
1165 significantly increased between E12.5 or E13.5 and E14.5 (Kruskall-Wallis test $P < 0.0001$;
1166 E12.5 versus E11.5 $P = 0.258$, E12.5 versus E13.5 $P = 0.904$, E12.5 versus E14.5 $P < 0.0001$,
1167 E12.5 versus E15.5 $P < 0.0001$, E12.5 versus E16.5 $P < 0.0001$, E13.5 versus E14.5 $P <$
1168 0.0001, E13.5 versus E15.5 $P < 0.0001$, E13.5 versus E16.5 $P < 0.0001$; E11.5 n = 31, E12.5
1169 n = 267, E13.5 n = 43, E14.5 n = 61, E15.5 n = 16, E16.5 n = 30). B. Graph showing how the
1170 input resistance R_{in} of $V1^R$ changes with embryonic age. R_{in} significantly increased between
1171 E12.5 or E14.5 and E15.5 (Kruskall-Wallis test $P < 0.0001$; E12.5 versus E11.5 $P > 0.999$,
1172 E12.5 versus E13.5 $P = 0.724$, E12.5 versus E14.5 $P > 0.999$, E12.5 versus E15.5 $P = 0.0004$,
1173 E12.5 versus E16.5 $P = 0.0005$, E14.5 versus E15.5 $P = 0.0019$, E14.5 versus E16.5 $P <$
1174 0.0058; E11.5 n = 31, E12.5 n = 261, E13.5 n = 43, E14.5 n = 60, E15.5 n = 16, E16.5 n = 30).
1175 C. Graph showing how the threshold of regenerative events (APs and plateau potentials) of
1176 $V1^R$ changes with embryonic age. The average threshold became significantly more
1177 hyperpolarized after E12.5 (Kruskall-Wallis test $P < 0.0001$; E12.5 versus E11.5 $P = 0.676$,
1178 E12.5 versus E13.5 $P = 0.0039$, E12.5 versus E14.5 $P < 0.0001$, E12.5 versus E15.5 $P <$
1179 0.0001, E12.5 versus E16.5 $P < 0.0001$, E13.5 versus E14.5 $P > 0.999$, E13.5 versus E15.5 P
1180 $= 0.1398$, E13.5 versus E16.5 $P = 0.0013$; E14.5 versus E15.5 $P > 0.999$, E14.5 versus E16.5
1181 $P = 0.0634$, E15.5 versus E16.5 $P > 0.999$; E11.5 n = 20, E12.5 n = 162, E13.5 n = 31, E14.5
1182 n = 30, E15.5 n = 16, E16.5 n = 30). Yellow and purple bars below the graphs indicate the
1183 two important phases of the functional development of spinal cord networks. The first one is

1184 characterized by synchronized neuronal activity (SNA) and the second one is characterized by
1185 the emergence of a locomotor-like activity (see text). Note that changes in C_{in} and
1186 R_{in} occurred at the end of the first developmental phase. (*P < 0.05, ** P < 0.01, *** P <
1187 0.001; control, E12.5).
1188
1189 **Fig 3. Developmental changes of embryonic V1^R firing patterns from E11.5 to E16.5.**
1190 The intrinsic activation properties were analyzed using 2 s suprathreshold depolarizing
1191 current steps. A-E. Representative traces of voltage responses showing SS V1^R (black), RS
1192 V1^R (red), ME V1^R (purple) and PP V1^R (blue) at E11.5 (A), E13.5 (B), E14.5 (C) E15.5 (D)
1193 and E16.5 (E). F. Bar graph showing how the proportions of the different firing patterns
1194 change from E11.5 to E16.5 (E11.5 n = 22, E12.5 n = 165, E13.5 n = 32, E14.5 n = 57, E15.5
1195 n = 15, 16.5 n = 28). Yellow and purple bars below the graphs indicate the first and the
1196 second phase of functional embryonic spinal cord networks. The proportions of the different
1197 firing patterns significantly changed between E11.5 to E12.5 (Fisher's exact test, P = 0.0052)
1198 with a significant increase in the proportion of RS V1^R (Fisher's exact test, P = 0.0336) and a
1199 significant decrease in the proportion of ME V1^R (Fisher's exact test, P = 0.01071) at E12.5.
1200 Only two firing patterns (SS and RS) were observed after E13.5 and most embryonic V1^R lost
1201 their ability to sustain tonic firing after E13.5. However, at E16.5 the proportion of RS V1^R
1202 significantly increased at the expense of SS V1^R when compared to E14.5 (Fisher's exact test,
1203 P = 0.0112), indicating that embryonic V1^R began to recover the ability to sustain tonic firing
1204 after E15.5.
1205
1206 **Fig 4**. **Activated caspase-3 is not observed in embryonic V1^R at E14.5.**
1207 Representative confocal image of the ventral part of an isolated lumbar spinal cord of
1208 E14.5 GAD67-eGFP mouse embryo showing immunostainings using antibodies against eGFP

1209 (A), FoxD3 (B) and activated Caspase 3 (aCaspace 3, C). D. Superimposition of the three
1210 stainings shows that embryonic $V1^R$ (eGFP+ and FoxD3+) were not aCaspase 3
1211 immunoreactive. A1, B1, C1 and D1. Enlarged images from A, B and C showing that
1212 aCaspase 3 staining is localized in areas where eGFP and Foxd3 stainings were absent. A2,
1213 B2, C2 and D2. Enlarged images from A, B and C showing that aCaspase 3 staining is absent
1214 in the area where $V1^R$ (eGFP+ and FoxD3+) are located. aCaspase 3 staining that did not co-
1215 localize with GAD67eGFP likely indicates MN developmental cell death [91].
1216
1217 **Fig 5. Delayed Rectifier and A-Type potassium currents are present in embryonic $V1^R$**
1218 **at E12.5.**
1219 Example of voltage-dependent potassium currents evoked in response to 10 mV membrane
1220 potential steps (200 ms) from -100 or from -30 mV to +40 mV (10 s interval between pulses).
1221 $V1^R$ were voltage clamped at V_H = -60 mV. A prepulse of -40 mV (300 ms) was applied to
1222 activate both I_A and I_{Kdr}. I_{Kdr} was isolated by applying a prepulse of 30 mV (300 ms) to
1223 inactivate I_A (A1 insert). I_A was isolated by subtracting step-by-step the currents obtained
1224 using a prepulse of 30 mV (V_H = - 30 mV) from the currents obtained using a prepulse of -40
1225 mV (V_H = -100 mV). A1, A3 and A5. Representative examples of the total outward K^+
1226 currents obtained from V_H = -100 mV (left traces), of I_{Kdr} (V_H = -30 mV, middle traces) and
1227 of isolated I_A (left traces) recorded at E12.5 in SS $V1^R$ (A1), RS $V1^R$ (A3) and PP $V1^R$ (A5).
1228 A2, A4 and A6. Current-voltage relationship ($I - V$ curves) of I_{Kdr} (filled circles) and of I_A
1229 (open circles) recorded in SS $V1^R$ (A2), RS $V1^R$ (A4) and PP $V1^R$ (A6) at E12.5. $I - V$ curves
1230 were obtained from currents shown in A1, A3 and A5. B1. Representative examples of the
1231 total outward K^+ currents obtained from V_H = -100 mV (left traces), of I_{Kdr} (V_H = -30 mV,
1232 middle traces) and of isolated I_A (left traces) recorded in SS $V1^R$ at E14.5. B2. Current-
1233 voltage relationship of I_{Kdr} (filled circle) and of I_A (open circle) in SS $V1^R$ at E14.5. $I -$

1234 V curves were obtained from currents shown in B1. Note that the $I - V$ curves are similar
1235 between SS V1^R, RS V1^R, PP V1^R at E12.5 and SS V1^R at E14.5.
1236
1237 **Fig 6. Maximal G_{Kdr}, G_{Nap} values and G_{Nap}/G_{Kdr} ratio in embryonic V1^R recorded at**
1238 **E12.5 and at E14.5.**
1239 A. Bar graph showing maximal G_{Kdr} value (Max G_{Kdr}) in SS V1^R at E12.5 (n = 9; gray bar)
1240 and at E14.5 (n = 10; gray bar), and in RS V1^R (n = 7; red bar), ME V1^R (n = 3; purple bar)
1241 and PP V1^R at E12.5 (n = 7; blue bar). G_{Kdr} was calculated from I_{Kdr} at V_H = + 20 mV,
1242 assuming a K^+ equilibrium potential of -96 mV. There is no significant difference
1243 in G_{Kdr} between SS V1^R and RS V1^R, while G_{Kdr} is significantly smaller in PP V1^R as
1244 compared to SS V1^R and RS V1^R. G_{Kdr} was significantly higher in SS V1^R at E14.5 than in SS
1245 V1^R, RS V1^R and PP V1^R at E12.5. (Kruskall-Wallis test $P < 0.0001$; SS V1^R versus RS V1^R
1246 at E12.5, $P = 0.5864$; SS V1^R versus PP V1^R at E12.5, $P = 0.0243$; RS V1^R versus PP V1^R at
1247 E12.5, $P = 0.0086$; E14.5 SS V1^R versus E12.5 SS V1^R, $P = 0.0048$; E14.5 SS V1^R versus
1248 E12.5 RS V1^R, $P = 0.0384$, E14.5 SS V1^R versus E12.5 PP V1^R, $P < 0.0001$). The increase in
1249 G_{Kdr} between E12.5 and E14.5 is likely to be due to the increase in neuronal size (input
1250 capacitance; Fig 2A). Indeed there was no significant difference (Mann Whitney test, P =
1251 0.133) in G_{Kdr} density between SS V1^R at E12.5 (408.5 ± 42.95 pS/pF, n = 9) and at E14.5
1252 (522.6 ± 49.6 pS/pF, n = 10). Bar graph showing the maximal G_{Nap} value (Max G_{Nap}) in SS
1253 V1^R at E12.5 (n 9; gray bar) and E14.5 (n = 10; green bar), and in RS V1^R (n = 8; red bar),
1254 ME V1^R (n = 3; purple bar) and PP V1^R (n = 6; blue bar) at E12.5. Max G_{Nap} was calculated
1255 from maximal I_{Nap} value measured on current evoked by depolarizing voltage ramp (see S3
1256 Fig), assuming a Na^+ equilibrium potential of +60 mV. There was no difference
1257 in G_{Nap} between RS V1^R and PP V1^R. On the contrary, G_{Nap} measured in SS V1^R at E12.5 or
1258 at E14.5 was significantly smaller as compared to G_{Nap} measured at E12.5 in RS V1^R or in PP

1259 V1^R. G_{Nap} measured at E12.5 and E14.5 in SS V1^R were not significantly different (Kruskall-
1260 Wallis test $P < 0.0001$; E12.5 SS V1^R versus E12.5 RS V1^R, $P = 0.0034$; E12.5 SS V1^R versus
1261 E12.5 PP V1^R, $P = 0.0006$; E12.5 RS V1^R versus E12.5 PP V1^R, $P = 0.5494$; E14.5 SS V1^R
1262 versus E12.5 SS V1^R, $P = 0.5896$; E14.5 SS V1^R versus E12.5 RS V1^R, $P = 0.0005$; E14.5 SS
1263 V1^R versus E12.5 PP V1^R, $P < 0.0001$). C. Histograms showing the G_{Nap} / G_{Kdr} ratio in SS
1264 V1^R at E12.5 (n = 9; gray bar) and E14.5 (n = 10; green bar) and in RS V1^R (n = 8; red bar),
1265 ME V1^R (n = 3; purple bar) and PP V1^R (n = 6; blue bar) at E12.5. Note that
1266 the G_{Nap} / G_{Kdr} ratio differs significantly between SS V1^R, RS V1^R and PP V1^R at E12.5,
1267 while it is not different between SS V1^R recorded at E12.5 and at E14.5 (Kruskall-Wallis test
1268 $P < 0.0001$; SS V1^R versus RS V1^R at E12.5, $P = 0.0367$; SS V1^R versus PP V1^R at E12.5, $P <$
1269 0.0001; RS V1^R versus PP V1^R at E12.5, $P = 0.0159$; E14.5 SS V1^R versus E12.5 SS V1^R, $P =$
1270 0.2319; E14.5 SS V1^R versus E12.5 RS V1^R, $P = 0.0017$; E14.5 SS V1^R versus E12.5 PP V1^R
1271 $P < 0.0001$). Data shown in A and B were used to calculate G_{Nap} / G_{Kdr} ratio shown in C. (*P
1272 < 0.05, ** $P < 0.01$, *** $P < 0.001$).
1273
1274 **Fig 7. Delayed Rectifier potassium current was inhibited by low concentrations of 4-**
1275 **aminopyridine in embryonic V1^R recorded at E12.5.**
1276 Example of voltage-dependent potassium currents evoked in response to 10 mV membrane
1277 potential steps (200 ms) from -100 mV or from -30 mV to +40 mV (10 s interval between
1278 pulses). V1 ^{R} were voltage clamped at V_H = -60 mV. A prepulse of -40 mV (300 ms) was
1279 applied to activate both I_A and I_{Kdr}.
1280 I_{Kdr} was evoked in response to 10 mV membrane potential steps (200 ms) from -100 mV to
1281 +40 mV. V1 ^{R} were voltage clamped at V_H = -60 mV. A prepulse of 30 mV (V_H = - 30 mV)
1282 was applied to isolate I_{Kdr}. A1. Representative example of the effect of 300 μM 4-AP
1283 application on I_{Kdr} recorded from embryonic V1^R at E12.5. A2. Curves showing current-

1284 voltage relationships of I_{Kdr} in control and in the presence of 300 μM 4-AP. Measurements
1285 were performed on traces shown in A1. B. Dose-response relationship of 4-AP-evoked I_{Kdr}
1286 inhibition (mean + SE). Data were normalized to I_{Kdr} amplitude measured in the absence of
1287 4-AP (V_H = 40mV) and fitted as explained in Materials and Methods. Note that 4-AP IC_{50} is
1288 in μM range (2.9 μM). 0.3 μM 4-AP n = 3, 1 μM 4-AP n = 3, 3 μM 4-AP n = 9, 10 μM 4-AP
1289 n = 13, 30 μM 4-AP n = 7, 100 μM 4-AP n = 7, 300 μM 4-AP n = 7.
1290
1291 **Fig 8. Increasing 4-AP concentration changed the firing pattern of single spiking**
1292 **embryonic $V1^R$ recorded at E12.5.**
1293 The firing pattern of embryonic $V1^R$ was evoked by 2 s suprathreshold depolarizing current
1294 steps. A1. Representative traces showing an example of the effect of increasing concentration
1295 of 4-AP (from 3 to 300 μM) on the firing pattern of a SS $V1^R$ recorded at E12.5. Note that in
1296 this case increasing 4-AP concentration converted single spiking (black trace) to repetitive
1297 spiking (red trace), repetitive spiking to a mixed event pattern (purple trace) and mixed events
1298 to plateau potential (blue trace). A2. Example of SS $V1^R$ in which increasing 4-AP
1299 concentration converted single spiking to repetitive spiking only. A3. Bar plots showing the
1300 change in the firing pattern of SS $V1^R$ according to 4-AP concentrations (control n = 10, 3 μM
1301 4-AP n = 8, 10 μM 4-AP n = 10, 30 μM 4-AP n = 10, 100 μM 4-AP n = 10, 300 μM 4-AP n =
1302 8). A4. Representative traces showing the effect of 0.5 μM TTX on a plateau potential evoked
1303 in a SS $V1^R$ in the presence of 300 μM 4-AP. A5. Representative traces showing the effect of
1304 0.5 μM TTX on repetitive AP firing evoked in a SS $V1^R$ in the presence of 300 μM 4-AP. In
1305 both cases, the application of TTX fully blocked the responses evoked in the presence of 4-
1306 AP, indicating that they were underlain by the activation of voltage-gated Na^+ channels. B1
1307 and B2. Representative traces showing the effect of 4-AP application (600 μM) on the firing
1308 pattern of single SS $V1^R$ recorded at E14.5. Note that the applications of 600 μM 4-AP

1309 evoked either a plateau potential (B1) or repetitive AP firing (B2), both fully blocked by TTX.
1310 B3. Bar plots showing the proportions of the different firing patterns observed in the presence
1311 of 600 μM 4-AP versus control recorded in SS $V1^R$ at E14.5 (n = 14).
1312
1313 **Fig 9. Embryonic $V1^R$ firing patterns predicted by computational modeling.**
1314 A. Firing patterns of 27 recorded cells, in which both G_{Nap} and G_{Kdr} were measured. Gray:
1315 SS, red: RS, blue: PP. The three purple points located at the boundary between the RS and PP
1316 regions correspond to mixed events (ME) where plateau potentials alternate with spiking
1317 episodes. Note that no cell exhibited low values of both G_{Nap} and G_{Kdr} (lower left), or large
1318 values of both conductances (upper right). B. Bifurcation diagram of the deterministic model
1319 when G_{Kdr} is kept fixed to 2.5 nS or 10 nS while G_{Nap} is varied. G_{in} = 1 nS and I = 20 pA.
1320 For G_{Kdr} = 10 nS (i.e. in the top experimental range), the red curves indicate the maximal and
1321 minimal voltages achieved on the stable limit cycle associated with repetitive firing (solid
1322 lines) and on the unstable limit cycle (dashed lines). The fixed point of the model is indicated
1323 by a gray solid line when it corresponds to the stable quiescent state, a gray dashed line when
1324 it is unstable and a solid blue line when it corresponds to a stable plateau potential. The two
1325 HB corresponding to the change of stability of the quiescence state (HB_1, G_{Nap}= 0.95 nS) and
1326 of the voltage plateau (HB_2, G_{Nap}= 3.04 nS) are indicated, as well as the two SN bifurcations
1327 of limit cycles associated with the onset (SN_1, G_{Nap} = 0.58 nS) and offset (SN_2, G_{Nap}= 3.14
1328 nS) of repetitive spiking as G_{Nap} is increased. For G_{Kdr} = 2.5 nS, the model does not display
1329 repetitive firing; it possesses a unique fixed point, which is always stable (blue-gray curve).
1330 The transition from quiescence to plateau is gradual with no intervening bifurcation.
1331 Representative voltage traces of the three different activity patterns are shown: single spiking
1332 in response to a 2 s current pulse (gray, G_{Nap} = 0.1 nS, G_{Kdr} = 10 nS), repetitive spiking
1333 (red, G_{Nap} = 1.5 nS, G_{Kdr} = 10 nS) and plateau potential (blue, G_{Nap} = 1.5 nS, G_{Kdr} = 2.5 nS).

1334 Note that the plateau never outlasts the current pulse. C. Bifurcation diagram when G_{Nap} is
1335 kept fixed at 1.5 nS and G_{Kdr} is varied (I = 20 pA). Same conventions as in B. Plateau
1336 potential is stable until point HB_2 (G_{Kdr} = 5.05 nS), repetitive firing can be observed between
1337 HB_2 and SN_1 (G_{Kdr} = 21.05 nS). The quiescent state is stable from point HB_1 (G_{Kdr} = 15.76
1338 nS) onward. Increasing G_{Nap} by merely 10% from 1.5 to 1.65 nS makes the bifurcation HB_2
1339 subcritical (not shown). This is because the RS-PP transition of the model occurs near a
1340 Bautin bifurcation (a.k.a. generalized HB) bifurcation, where the supercritical HB, subcritical
1341 HB and the SN bifurcation of limit cycles merge as shown in D (point B_2). D. Two-
1342 parameters bifurcation diagram of the model in the G_{Nap} - G_{Kdr} plane (I = 20 pA). The black
1343 lines indicate the bifurcations HB_1 and HB_2. The red lines indicate the SN bifurcations of
1344 limit cycles SN_1 and SN_2. The shaded area indicates the region where repetitive firing can
1345 occur. The black squares B_1 and B_2 correspond to Bautin bifurcations where supercritical HB
1346 (occurring between B_1 and B_2), subcritical HB (occurring on the rest of the HB_1 and HB_2 lines)
1347 and the SN bifurcations of limit cycles SN_1 and SN_2 coalesce. Because the model is near a
1348 Bautin bifurcation, its behavior is little affected by the nature of the bifurcation HB_2. When
1349 HB_2 is subcritical, the bistability region between HB2 and SN_2 is narrow (see Fig 9, B and D)
1350 and action potentials keep a large amplitude until their disappearance at point HB_2 (see Fig
1351 9B). When HB_2 is supercritical, the spike amplitude vanishes at HB_2 but the decay is very
1352 steep (see Fig 9C). Taking into account channel noise further softens the distinction between
1353 these two cases. The oblique lines correspond to three different values of the ratio G_{Nap}/G_{Kdr}:
1354 0.03 (gray), 0.2 (red) and 0.5 (blue). Voltage traces on the right display the response to a 2 s
1355 current pulse when channel noise is taken into account for the three regimes: quiescence (top,
1356 gray trace and dot in the diagram), repetitive firing (middle, red) and plateau potential (bottom,
1357 blue). They correspond to the three deterministic voltage traces shown in B. Note that the
1358 one-parameter bifurcation diagrams shown in B correspond to horizontal lines through points

1359 1 and 2 (G_{Kdr} = 10 nS) and through point 3 (G_{Kdr} = 2.5 nS), respectively. The bifurcation
1360 diagram in C corresponds to a vertical line through point 2 and 3 (G_{Nap} = 1.5 nS). E.
1361 Cumulative distribution function of the ratio G_{Nap}/G_{Kdr} for the four clusters shown in A,
1362 showing the sequencing SS (gray) → RS (red) → ME (purple, 3 cells only) → PP (blue)
1363 predicted by the two-parameters bifurcation diagram in D. The wide PP range, as compared to
1364 SS and RS, merely comes from the fact that G_{Kdr} is small for cells in this cluster. F. The data
1365 points in A are superimposed on the two-parameters bifurcation diagram shown in D,
1366 demonstrating that our basic model accounts well for SS, RS and PP clusters (indicated with
1367 the same color code as in A). The bifurcation diagram is simplified compared to A, only the
1368 region where repetitive spiking is possible (i.e. between the lines SN_1 and SN_2 in A) being
1369 displayed (shaded area). Notice that 3 ME cells (purple dots) are located near the transition
1370 between the RS and PP regions (indicated here by the purple fringe along the SN_2 bifurcation
1371 line). The four arrows indicate the presumable evolution of G_{Nap} and G_{Kdr} for SS, RS, ME
1372 and PP cells between E12.5 and E14.5-15.5. G_{Nap} eventually decreases while G_{Kdr} keeps on
1373 increasing. G. Distribution of a sample of cells in the G_{Kdr} - G_{Kdr} plane at E14.5. All the cells
1374 are located well within the SS region far from bifurcation lines because of the decreased G_{Nap}
1375 compared to E12.5, the increased G_{Kdr}, and the shift of the RS region (shaded) due to
1376 capacitance increase (18 versus 13 pF).
1377
1378 **Fig 10. Effects of the slow inactivation of I_{Nap} on firing patterns predicted by**
1379 **computational modeling.**
1380 A. Examples of repetitive plateaus (left) and mixed events (right) recorded in $V1^R$ at E12.5
1381 during a 2 s current pulse. B1. Current-voltage curve of the basic model (without slow
1382 inactivation of I_{Nap}, and without I_A or channel noise) for G_{Kdr} = 2.5 nS and for G_{Nap} = 1.7 nS
1383 (lower curve) and 2.5 nS (upper curve). G_{in} = 2.5 nS. Solid lines denote stable fixed points

1384 and dashed lines unstable ones. For G_{Nap} =1.7 nS, bistability between quiescence and plateau
1385 occurs between the SN bifurcations SN_1 (I = 2.1 pA) and SN_2 (I = 8.3 pA). When G_{Nap} is
1386 increased to 2.5 nS, that bistability region extends to the negative current range, which
1387 implies that once a plateau has been elicited, the model will stay in that stable state and not
1388 return to the resting state, even though current injection is switched off (see insert). B1 Insert.
1389 Voltage response to a 2 s current pulse of 8 pA for G_{Nap} = 2.5 nS. The resting state (gray dot
1390 on the lower curve in B1) is destabilized at pulse onset and a plateau is elicited (blue dot on
1391 the upper curve in B1). At pulse offset, the plateau is maintained, even though the injected
1392 current is brought back to zero, and channel noise is not sufficient to go back to the resting
1393 state. B2. Domain of bistability between quiescence and plateau (shaded) in the I- G_{Nap} plane
1394 for G_{Kdr}= 2.5 nS. It is delimited by the two lines SN_1 and SN_2 where SN bifurcations of fixed
1395 points occur. Bistability requires that G_{Nap} exceeds 1.35 nS, and the domain of bistabilty
1396 enlarges as G_{Nap} is increased further. The two horizontal lines correspond to the two cases
1397 shown in B1: G_{Nap} =1.7 nS and 2.5 nS. C. Behavior of the model when slow inactivation is
1398 incorporated (half-inactivation voltage V_s = -30 mV, steepness k_s= -5 mV). The bifurcation
1399 diagram of the basic model (without slow inactivation) for I = 8 pA (compared to 20 pA in
1400 Fig 9) and G_{Kdr} = 2.5 nS (same conventions as in Fig 9B) and the stable limit cycle (black
1401 solid curve) obtained when slow inactivation is added (voltage-independent time constant: 1 s)
1402 are superimposed. The limit cycle is comprised of four successive phases (see labels): 1) long
1403 plateau during which I_{Nap} slowly inactivates, 2) fast transition to the quiescent state, 3)
1404 repolarization episode during which I_{Nap} slowly deinactivates, 4) fast transition back to the
1405 plateau. Each plateau starts with a full blown action potential (or a series of rapidly decaying
1406 spikelets). Note that the bifurcation HB is subcritical here (unstable limit cycle in red), at
1407 variance with square wave bursting (supercritical bifurcation and stable limit cycle); this is a
1408 characteristic feature of pseudo-plateau bursting. Voltage responses to a 2 s current pulse are

1409 shown on the right for different kinetics of slow inactivation. Top: voltage-independent time
1410 constant of 1 s, Middle: same with channel noise added to fast and slow gating variables,
1411 Bottom: time constant increases with membrane voltage from 100 ms to 1 s (midpoint: -30
1412 mV, steepness: 15 mV), D. Mixed events. The bifurcation diagram of the basic model
1413 for G_{Kdr} = 2.5 nS and I = 10 pA and the stable limit cycle obtained in the presence of slow
1414 inactivation (G_{Nap} = 2.5 nS, V_s = -20 mV, k_s = -15 mV, voltage-independent time constant: 1
1415 s) are superimposed. Here again, the limit cycle is comprised of four successive phases (see
1416 labels): 1) slow inactivation of I_{Nap} that leads to the crossing of the bifurcation point HB_2 and
1417 the destabilization of the plateau potential, 2) fast transition to the spiking regime, 3)
1418 repetitive spiking during which I_{Nap} slowly de-inactivates, which leads to the crossing of the
1419 bifurcation point SN_2 and terminates the spiking episode, 4) fast transition back to the stable
1420 plateau potential. Voltage traces for a constant injected current (10 pA) are shown on the right
1421 and in the absence of any channel noise. Top: voltage-independent time constant of 1 s,
1422 Bottom: time constant increases with membrane voltage from 200 to 800 ms (same V_s and k_s
1423 as in C). Note that in C and D the first plateau lasts longer than the following ones, as in
1424 electrophysiological recordings of embryonic $V1^R$ cells displaying repetitive plateaus. This
1425 form of adaptation is caused by the slow inactivation of the persistent sodium current.
1426

1427 **Fig 11. Effect of 4-AP application on evoked GABAergic GICs or GDPs recorded in**
1428 **MNs at E12.5.**

1429 Drawing showing the cervical position of the stimulation electrode and the lumbar position of
1430 the recording electrode. B. Evoked Giant Inward Current (GIC) in the presence of 4 mM
1431 kynurenic acid in control condition, in the presence of 30 μM 4-AP and 300 μM 4-AP. B1.
1432 Representative example of GICs in the three conditions. B2. Bar graph showing GIC
1433 amplitude (pA) and half-width (s) (*P < 0.05). 4-AP applied at concentrations of 30 μM or

1434 300 μM significantly increased the amplitude (Wilcoxon test, P = 0.016 and P = 0.047
1435 respectively) and half-width (Wilcoxon test, P = 0.016 and P = 0.018 respectively) of
1436 GABAergic GIC. C. Evoked Giant Depolarizing Potential (GDP) in the presence of 4 mM
1437 kynurenic acid in control condition, in the presence of 30 μM 4-AP and 300 μM 4-AP. C1.
1438 Representative example of GDPs in the three conditions. C2. Bar graph showing GDPs
1439 amplitude (mV) and half-width (s). 4-AP applied at concentrations of 30 μM or 300 μM
1440 significantly increased GABAergic GDPs half-width (Wilcoxon test P = 0.004 and P = 0.007
1441 respectively), but it did not significant change the amplitude (Wilcoxon test P = 0.07 and P =
1442 0.07 respectively).
1443

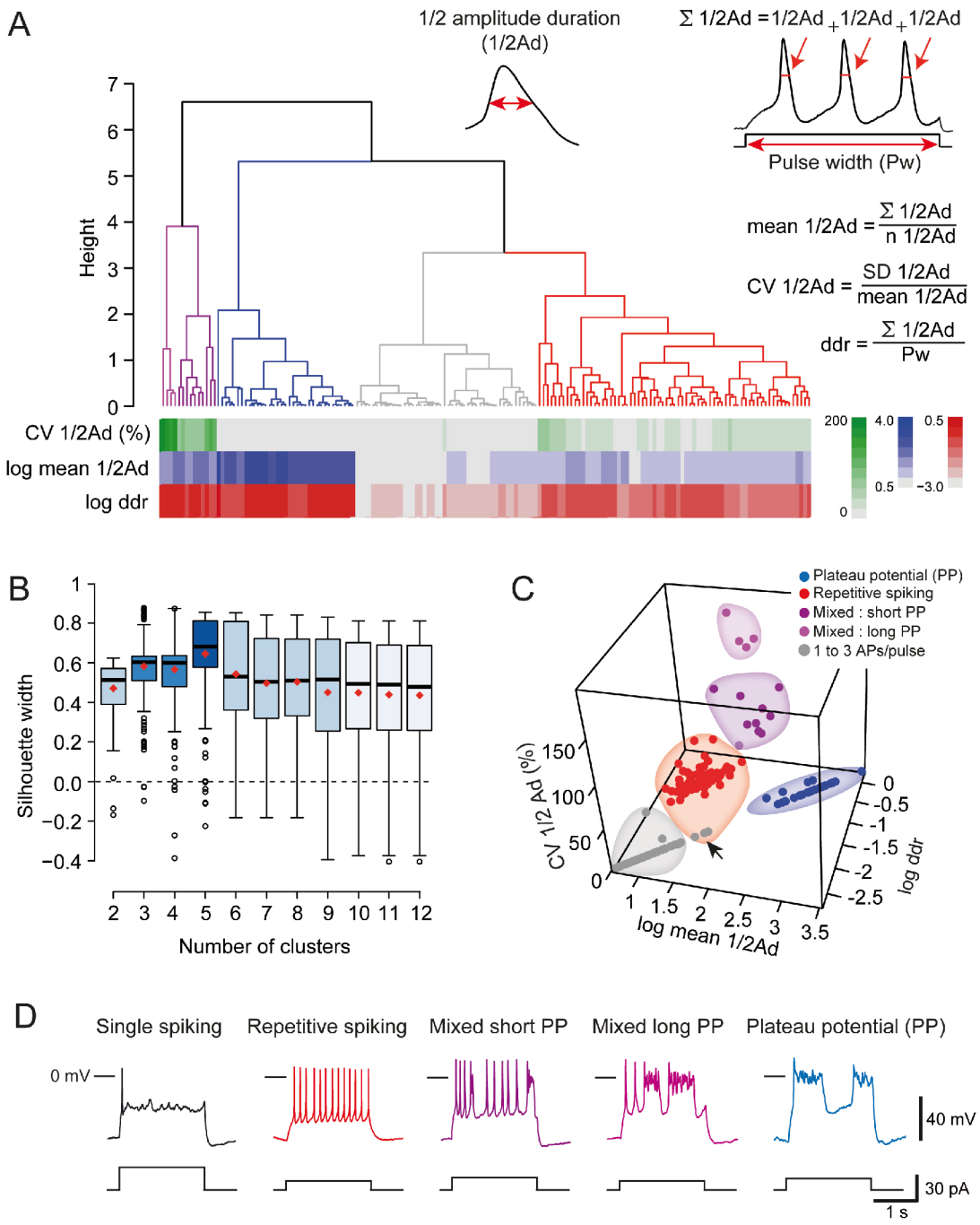
A
1/2 amplitude duration
(1/2Ad)
Σ 1/2Ad =1/2Ad +1/2Ad +1/2Ad
Pulse width (Pw)
mean 1/2Ad = Σ 1/2Ad / n 1/2Ad
CV 1/2Ad = SD 1/2Ad / mean 1/2Ad
ddr = Σ 1/2Ad / Pw
Height
CV 1/2Ad (%)
log mean 1/2Ad
log ddr
B
Silhouette width
Number of clusters
C
Plateau potential (PP)
Repetitive spiking
Mixed : short PP
Mixed : long PP
1 to 3 APs/pulse
CV 1/2 Ad (%)
log mean 1/2Ad
log ddr
D
Single spiking
Repetitive spiking
Mixed short PP
Mixed long PP
Plateau potential (PP)
0 mV
40 mV
30 pA
1 s

Fig 1.

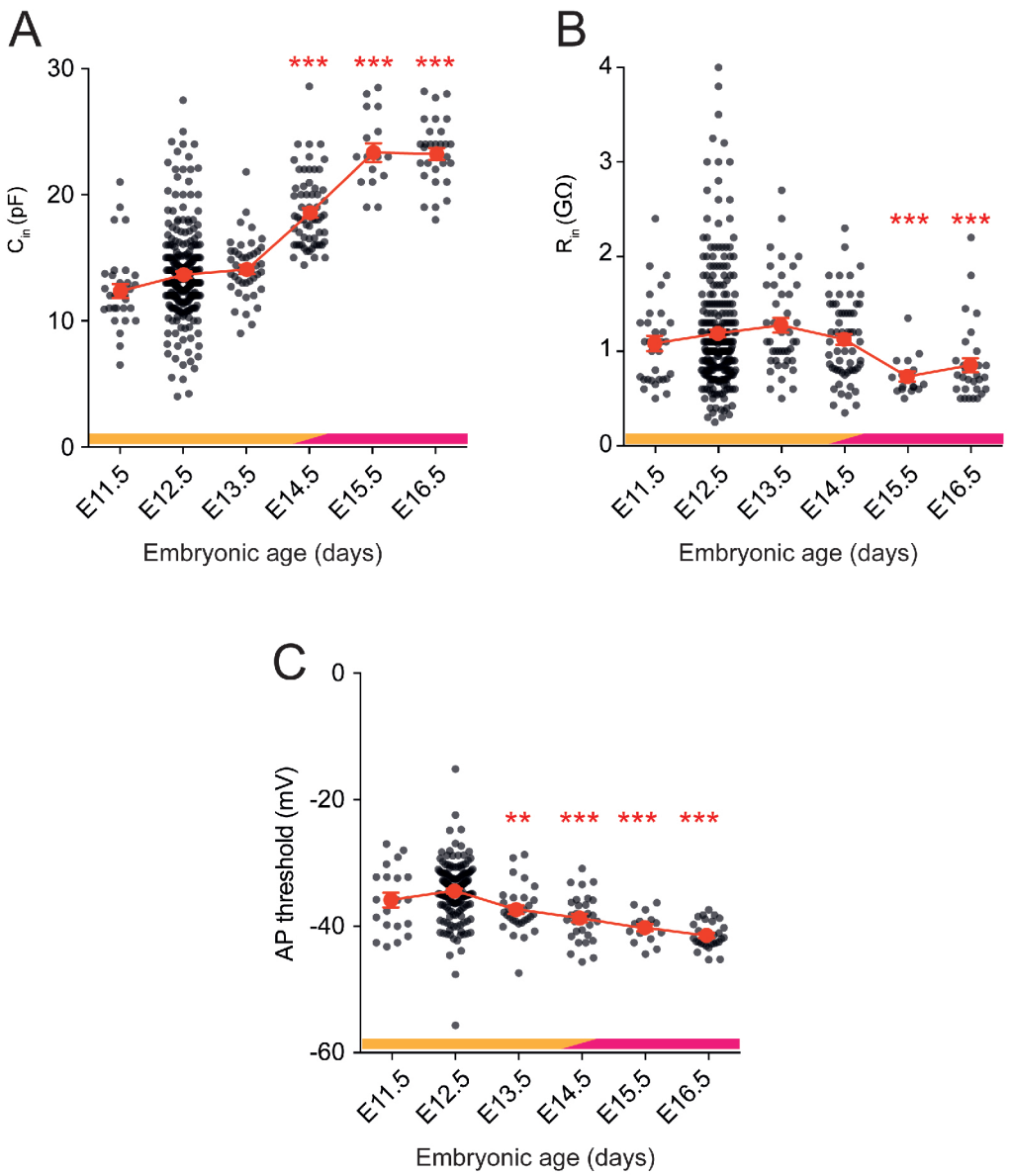
A
30
20
10
0
C_{in} (pF)
***
***
***
E11.5
E12.5
E13.5
E14.5
E15.5
E16.5
Embryonic age (days)
B
4
3
2
1
0
R_{in} (GΩ)
***
***
E11.5
E12.5
E13.5
E14.5
E15.5
E16.5
Embryonic age (days)
C
0
-20
-40
-60
AP threshold (mV)
**
***
***
***
E11.5
E12.5
E13.5
E14.5
E15.5
E16.5
Embryonic age (days)

Fig 2.

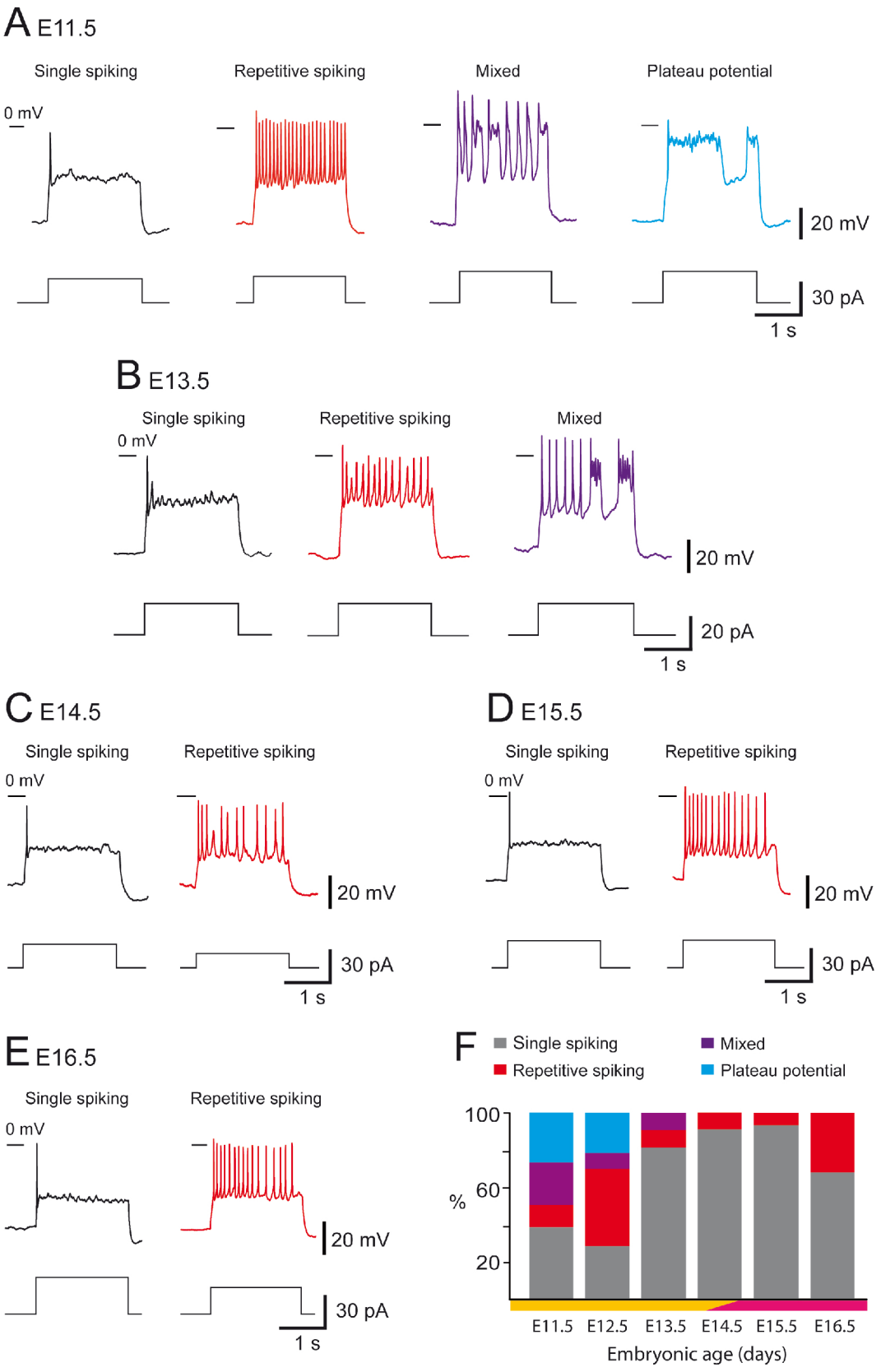
A E11.5
Single spiking
Repetitive spiking
Mixed
Plateau potential
0 mV
20 mV
30 pA
1 s
B E13.5
Single spiking
Repetitive spiking
Mixed
0 mV
20 mV
20 pA
1 s
C E14.5
Single spiking
Repetitive spiking
0 mV
20 mV
30 pA
1 s
D E15.5
Single spiking
Repetitive spiking
0 mV
20 mV
30 pA
1 s
E E16.5
Single spiking
Repetitive spiking
0 mV
20 mV
30 pA
1 s
F
Single spiking
Mixed
Repetitive spiking
Plateau potential
100
60
20
%
E11.5
E12.5
E13.5
E14.5
E15.5
E16.5
Embryonic age (days)

Fig 3.

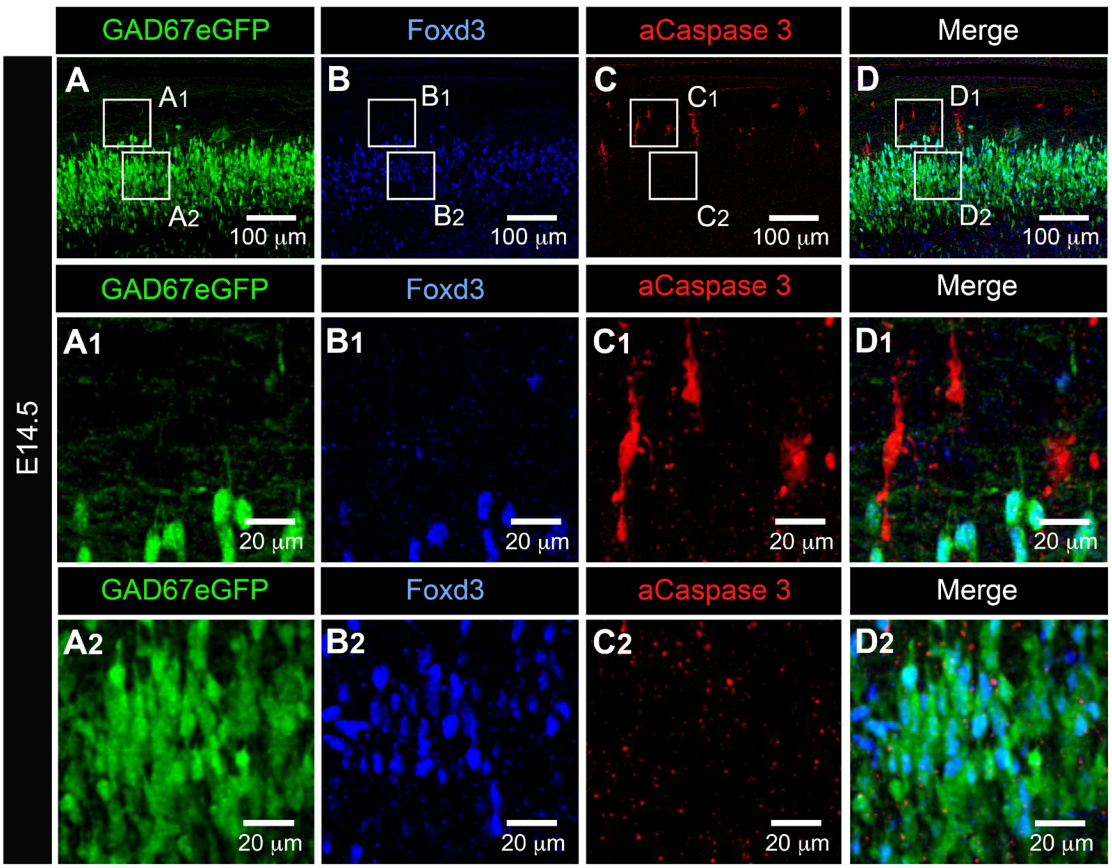
GAD67eGFP
Foxd3
aCaspase 3
Merge
E14.5
A
A1
A2
100 μm
B
B1
B2
100 μm
C
C1
C2
100 μm
D
D1
D2
100 μm
A1
B1
C1
D1
20 μm
A2
B2
C2
D2
20 μm

Fig 4.

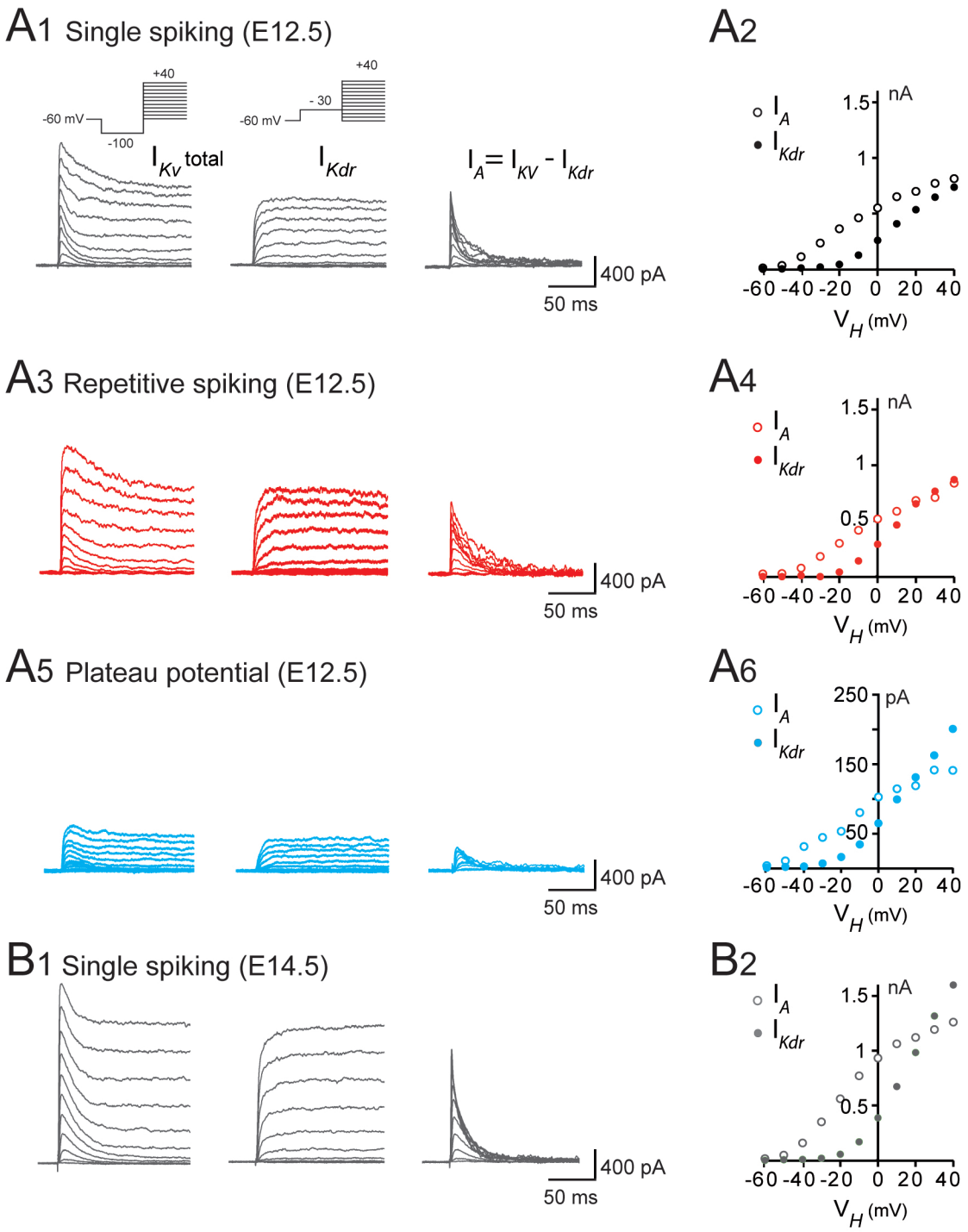
A1 Single spiking (E12.5)
+40
-60 mV
-100
+40
- 30
-60 mV
I Kv total
I Kdr
I A = I KV - I Kdr
400 pA
50 ms
A2
I A
I Kdr
1.5
nA
1
-60 -40 -20 0 20 40
V H (mV)
A3 Repetitive spiking (E12.5)
400 pA
50 ms
A4
I A
I Kdr
1.5
nA
1
0.5
-60 -40 -20 0 20 40
V H (mV)
A5 Plateau potential (E12.5)
400 pA
50 ms
A6
I A
I Kdr
250
pA
150
50
-60 -40 -20 0 20 40
V H (mV)
B1 Single spiking (E14.5)
400 pA
50 ms
B2
I A
I Kdr
1.5
nA
1
0.5
-60 -40 -20 0 20 40
V H (mV)

Fig 5.

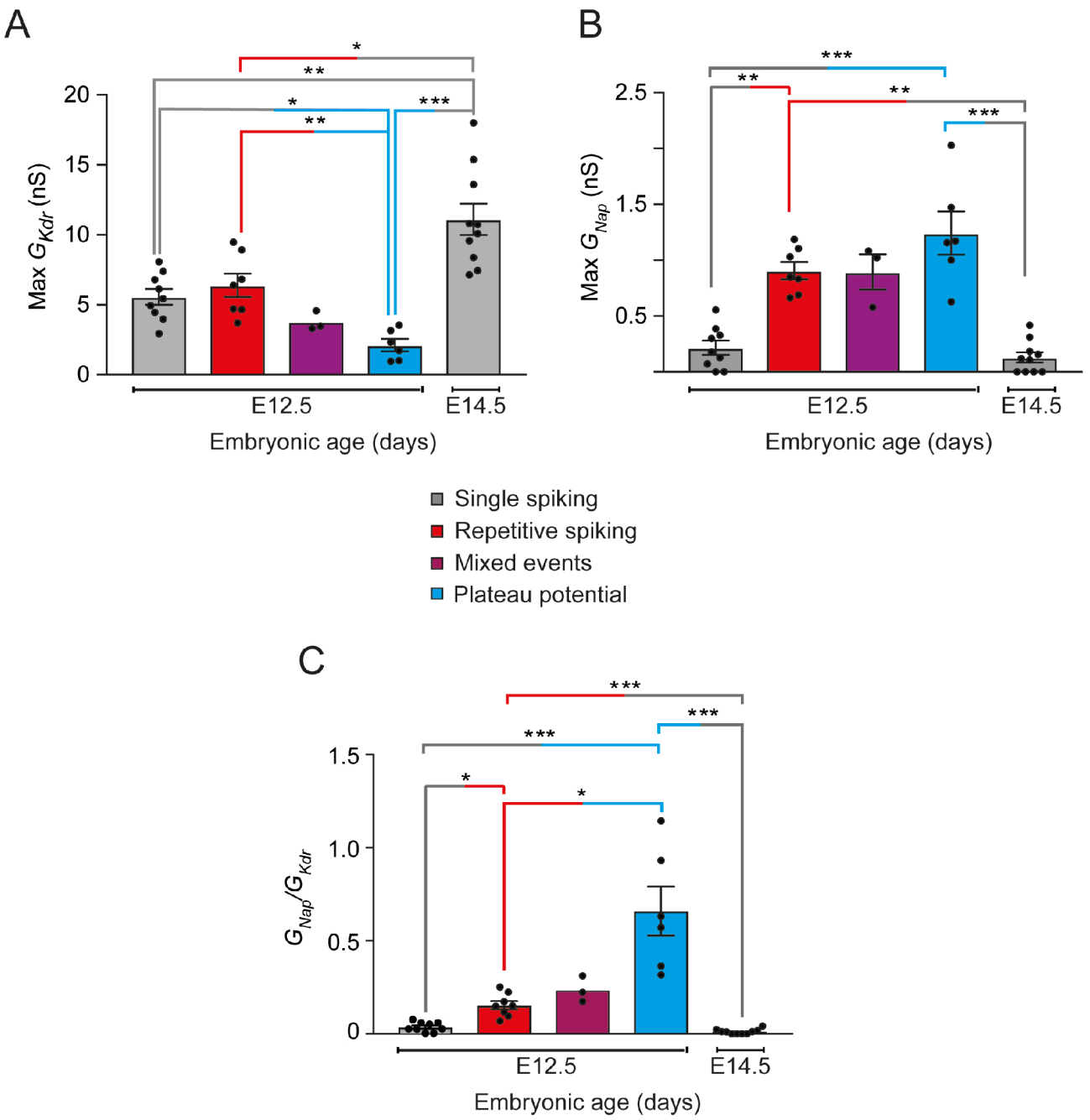
A
Max G_{Kdr} (nS)
20
15
10
5
0
*
**
*
**
***
E12.5
E14.5
Embryonic age (days)
B
Max G_{Nap} (nS)
2.5
1.5
0.5
***
**
**
***
E12.5
E14.5
Embryonic age (days)
Single spiking
Repetitive spiking
Mixed events
Plateau potential
C
G_{Nap}/G_{Kdr}
1.5
1.0
0.5
0
***
***
***
*
*
E12.5
E14.5
Embryonic age (days)

Fig 6.

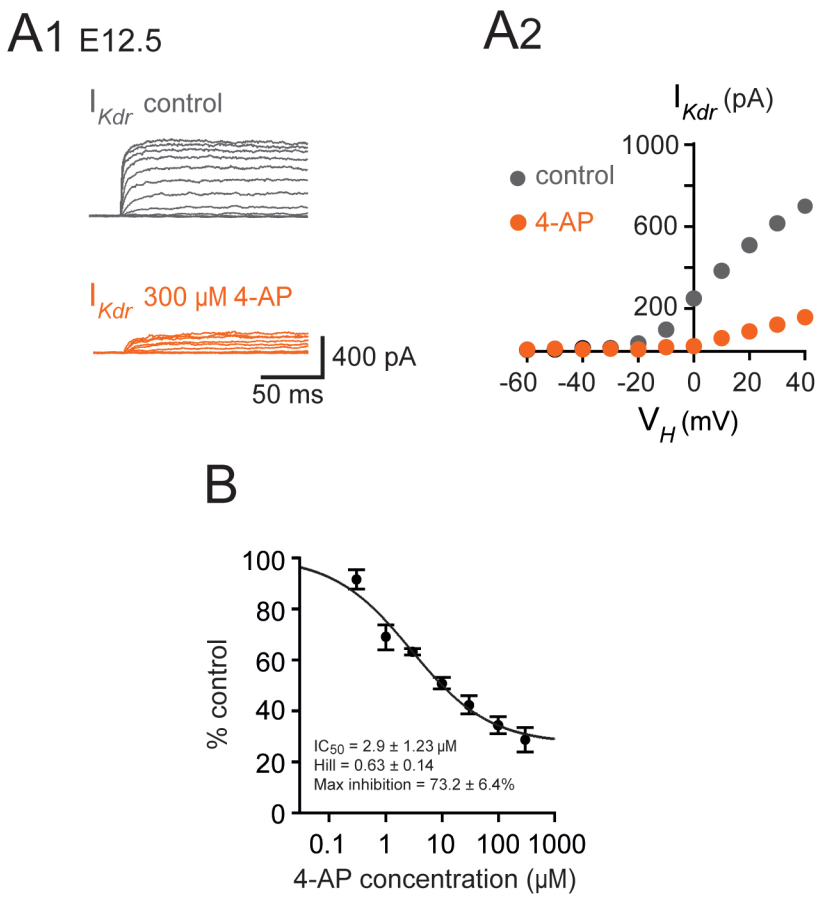
A1 E12.5
I Kdr control
I Kdr 300 μM 4-AP
400 pA
50 ms
A2
I Kdr (pA)
1000
600
200
control
4-AP
-60 -40 -20 0 20 40
V H (mV)
B
100
80
60
40
20
0
% control
IC50 = 2.9 ± 1.23 μM
Hill = 0.63 ± 0.14
Max inhibition = 73.2 ± 6.4%
0.1 1 10 100 1000
4-AP concentration (μM)

Fig 7.

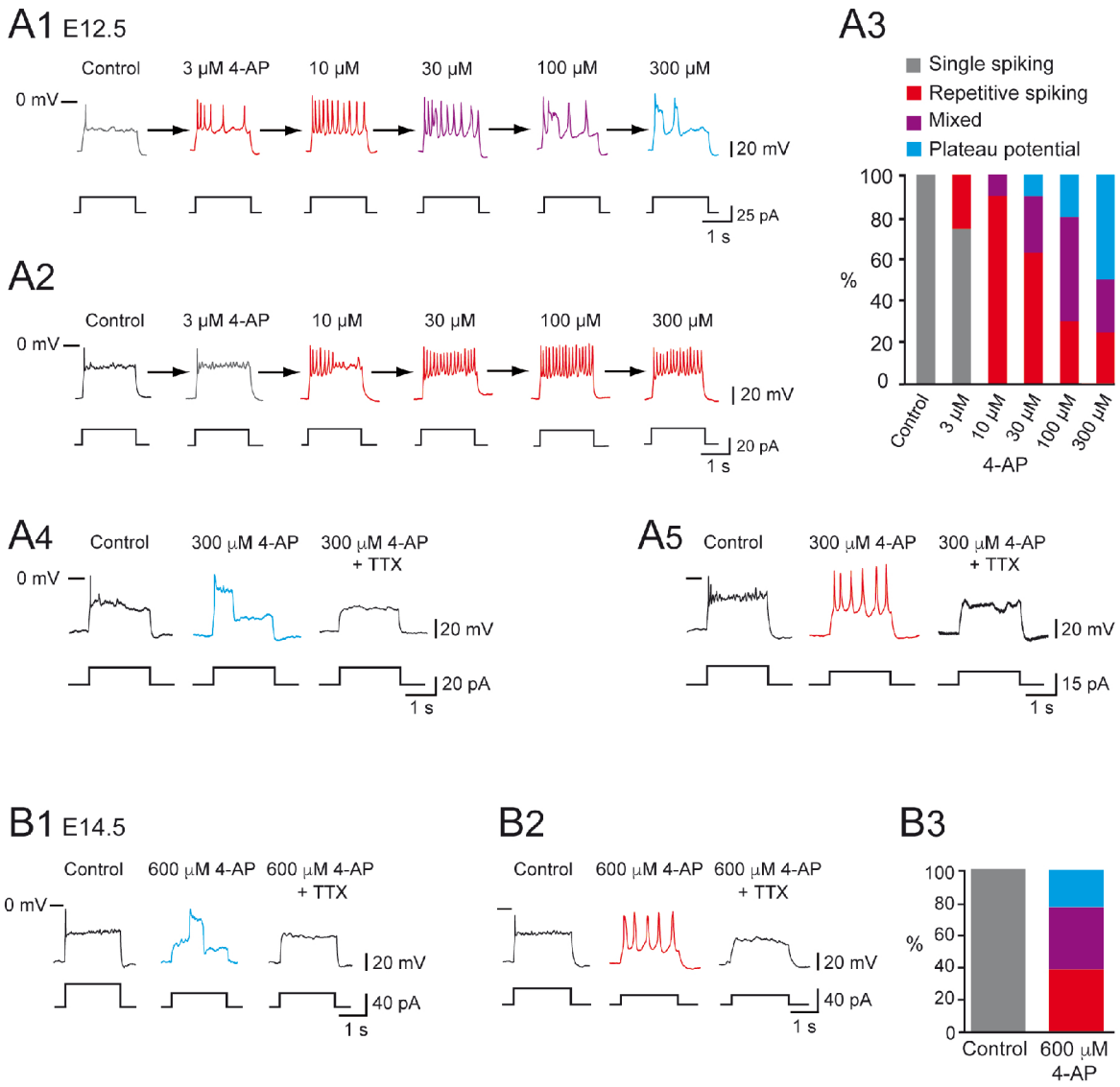
A1 E12.5
Control
3 μM 4-AP
10 μM
30 μM
100 μM
300 μM
0 mV
20 mV
25 pA
1 s
A2
Control
3 μM 4-AP
10 μM
30 μM
100 μM
300 μM
0 mV
20 mV
20 pA
1 s
A3
Single spiking
Repetitive spiking
Mixed
Plateau potential
100
80
60
40
20
0
%
Control
3 μM
10 μM
30 μM
100 μM
300 μM
4-AP
A4
Control
300 μM 4-AP
300 μM 4-AP
+ TTX
0 mV
20 mV
20 pA
1 s
A5
Control
300 μM 4-AP
300 μM 4-AP
+ TTX
20 mV
15 pA
1 s
B1 E14.5
Control
600 μM 4-AP
600 μM 4-AP
+ TTX
0 mV
20 mV
40 pA
1 s
B2
Control
600 μM 4-AP
600 μM 4-AP
+ TTX
20 mV
40 pA
1 s
B3
100
80
60
40
20
0
%
Control
600 μM
4-AP

Fig 8.

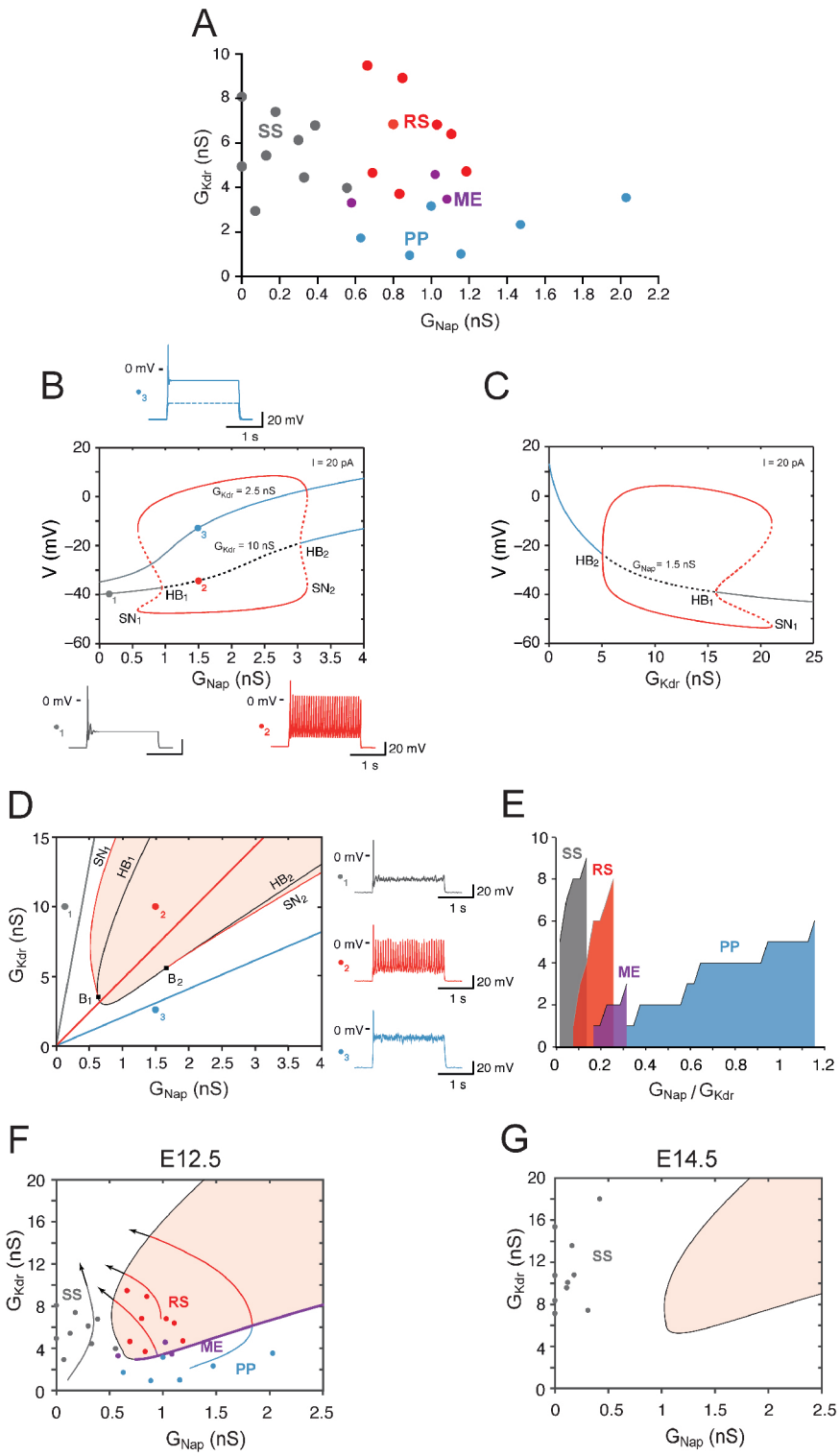
A
SS
RS
ME
PP
G_{Kdr} (nS)
G_{Nap} (nS)
B
0 mV
20 mV
1 s
I = 20 pA
G_{Kdr} = 2.5 nS
G_{Kdr} = 10 nS
HB2
HB1
SN2
SN1
V (mV)
G_{Nap} (nS)
C
I = 20 pA
HB2
G_{Nap} = 1.5 nS
HB1
SN1
V (mV)
G_{Kdr} (nS)
D
SN1
HB1
HB2
SN2
B1
B2
G_{Kdr} (nS)
G_{Nap} (nS)
E
SS
RS
ME
PP
G_{Nap} / G_{Kdr}
F
E12.5
SS
RS
ME
PP
G_{Kdr} (nS)
G_{Nap} (nS)
G
E14.5
SS
G_{Kdr} (nS)
G_{Nap} (nS)

Fig 9.

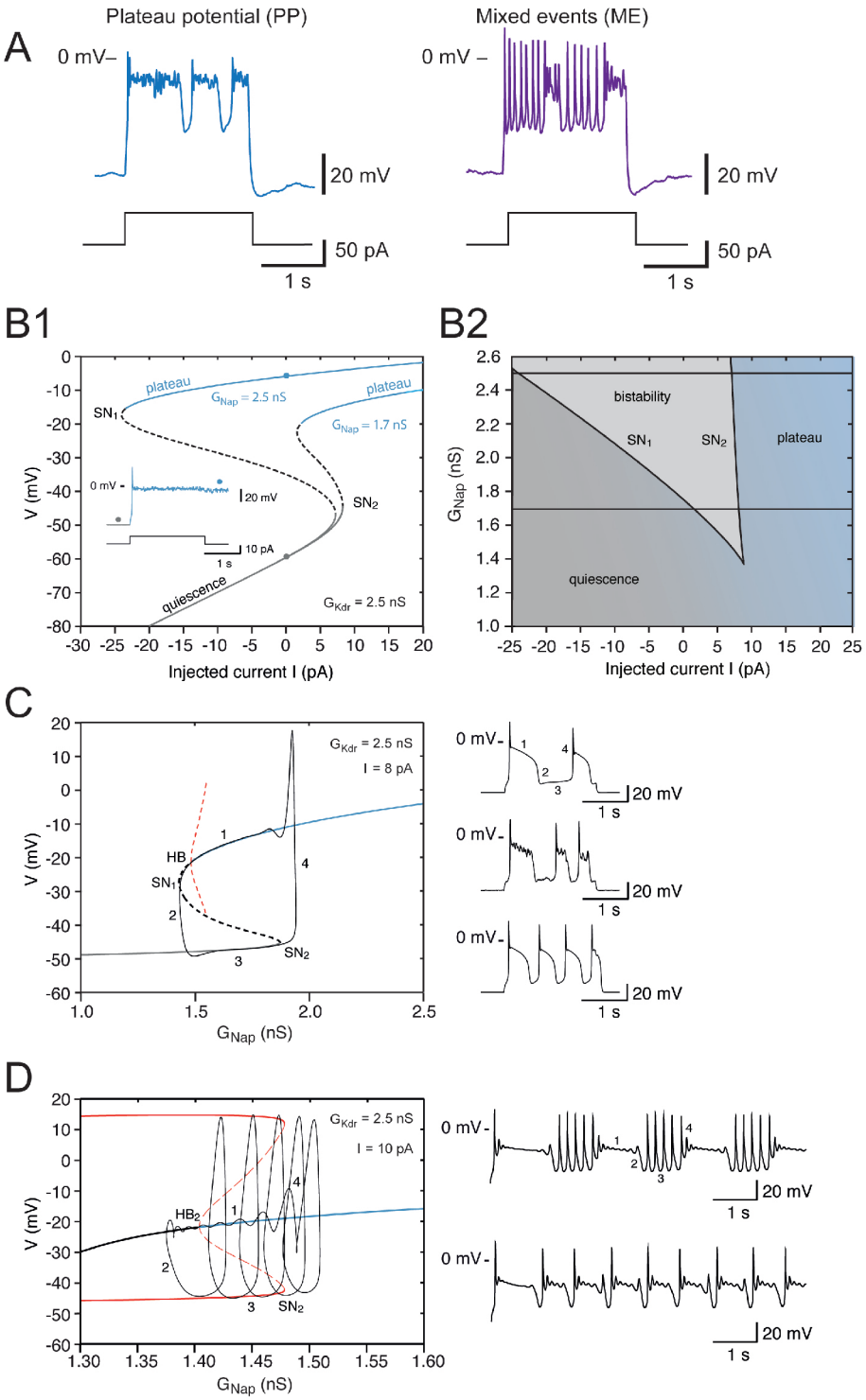
A
Plateau potential (PP)
Mixed events (ME)
0 mV
20 mV
50 pA
1 s
B1
B2
plateau
G_{Nap} = 2.5 nS
G_{Nap} = 1.7 nS
SN_1
SN_2
quiescence
G_{Kdr} = 2.5 nS
10 pA
V (mV)
Injected current I (pA)
bistability
G_{Nap} (nS)
C
I = 8 pA
HB
D
I = 10 pA
HB_2

Fig 10.

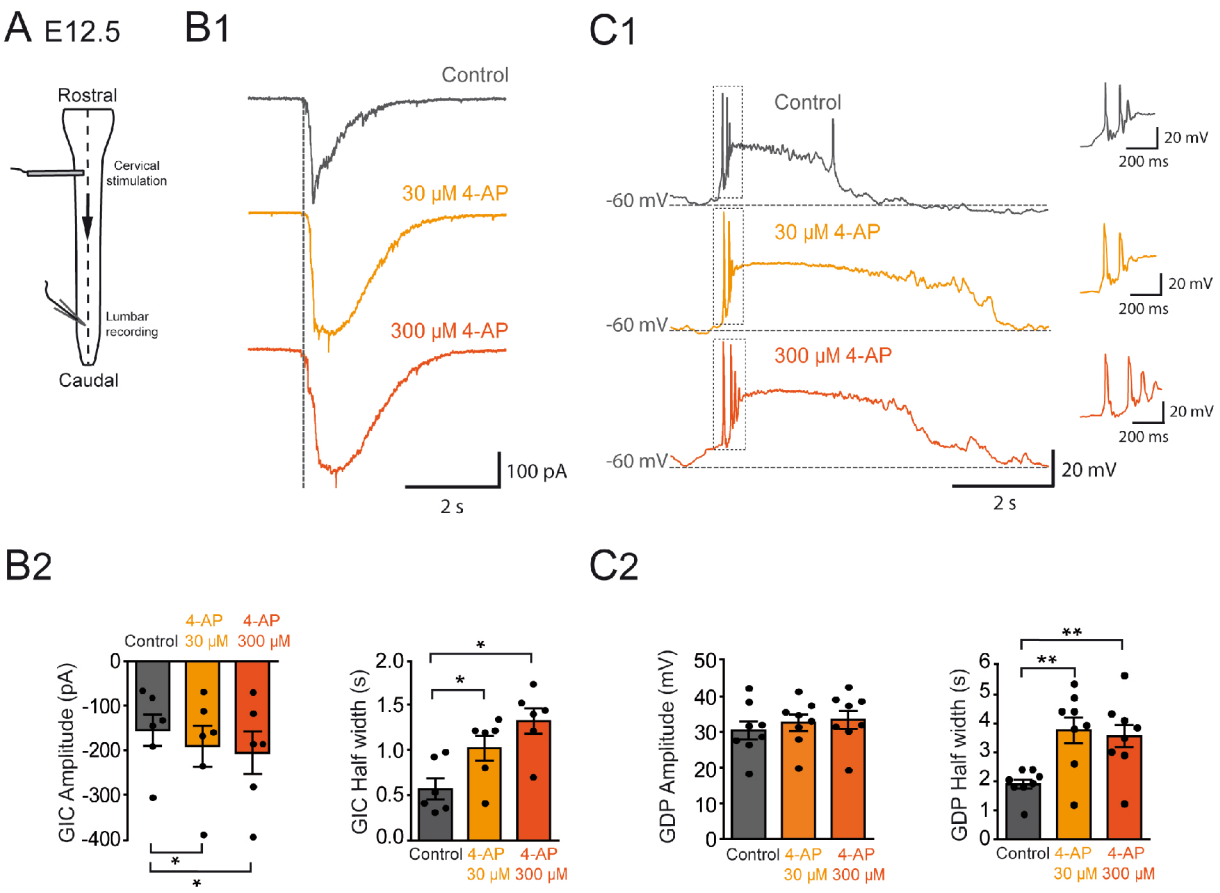
A E12.5
Rostral
Cervical stimulation
Lumbar recording
Caudal
B1
Control
30 μM 4-AP
300 μM 4-AP
100 pA
2 s
C1
Control
30 μM 4-AP
300 μM 4-AP
-60 mV
20 mV
200 ms
2 s
B2
Control
4-AP 30 μM
4-AP 300 μM
GIC Amplitude (pA)
GIC Half width (s)
C2
GDP Amplitude (mV)
GDP Half width (s)

Fig 11.